Neutral Xenon Density in the SPT-140 Near-Field Plume

IEPC-2013-399

Presented at the 33rd International Electric Propulsion Conference,
The George Washington University • Washington, D.C. • USA
October 6 – 10, 2013

M.W. Crofton,[a] A.G. Hsu Schouten,[b] J.A. Young,[c] E.J. Beiting,[d] and K.D. Diamant[e]
The Aerospace Corporation, El Segundo, California 90245, USA

R.L. Corey[f] and J.J. Delgado[g]
Space Systems/Loral, Palo Alto, CA 94303, USA

Density measurements of neutral xenon in the ground state were performed in the SPT-140 plume at 3 and 4.5 kW operating points. Cold flow results indicated significant density asymmetry between left and right channels on the thruster mid-line. Averaging out the asymmetry and integrating the differential flux to obtain total mass flux produced a close match with the known anode mass flow rate. Average hot flow neutral density across the thruster mid-line exit plane was nearly two orders of magnitude below the cold flow result, consistent with high ionization efficiency and elevated exit velocity under operating conditions. Neutral density was found to vary strongly across the face of the operating thruster, with prominent peaks at inner and outer edges of the annulus, dips below background levels and highest levels near the hollow cathode orifice. Jets of fast-moving neutral atoms emerge at the annular edges, with beam center pointed well away from the thrust axis. The jet velocity is much higher than thermal velocity at anode or thruster wall temperatures, and may result from the combined effects of preferential slow neutral ionization, ion-wall collisions and ion-neutral charge exchange. A similar explanation may apply to even higher neutral velocity observed in the cathode plume. Axial density profiles also reveal complex behavior, further suggesting that neutral depletion occurs in significant portions of the plume and that a neutral ionization mechanism is active in the plasma flow traveling away from the exit plane. Electron impact ionization and/or ion-neutral collisions are the likely causes of the neutral depletion. Cold background gas will diffuse into the ion beam over its length, acting to partially replenish neutral populations. Conversion of fast ions into slower ions via ion-neutral collisions and subsequent acceleration in the local electric field may increase total plume momentum and registered thrust.

I. Introduction

The first measurement of absolute, spatially-resolved neutral xenon density in the near-field plume of an operating Hall thruster has been performed. Two-photon laser absorption was used to excite ground state xenon

[a] Senior Scientist, Propulsion Science Department, M2-341, mark.w.crofton@aero.org, Senior Member AIAA.
[b] Member of the Technical Staff, Space Materials Laboratory, M2-341, Member AIAA.
[c] Member of the Technical Staff, Space Materials Laboratory, M2-341, Member AIAA.
[d] Senior Scientist, Space Materials Laboratory, M2-341, Associate Member AIAA.
[e] Research Scientist, Space Materials Laboratory, M2-341, Member AIAA.
[f] SPT Subsystem Lead Engineer, Propulsion Products, 3825 Fabian Way, M/S G86.
[g] Engineering Specialist, Propulsion Products, 3825 Fabian Way, M/S G86.

atoms to an upper state, which fluoresced at relatively long wavelengths as it transitioned quickly to other levels. This method is non-intrusive, and amenable to measurements throughout the plume if signal levels are adequate. Neutral density near an operating thruster is low; atmospheric density is more than 1 million times greater at all plume coordinates except near the cathode exit. Because Hall thrusters efficiently ionize the xenon propellant, the operational neutral plume density is much below the "cold flow" density levels established with discharge off, and identical flow rate. Because this factor is coupled with the small absorptivity of two-photon transitions and background emission from the plume, the measurement is challenging.

Emission spectroscopy and laser-based methods that probe excited states rather than ground states suffer from the variability of excited state populations throughout the plume. Excited state populations are sensitive to local conditions and typically do not follow a simple equilibrium distribution function, making the accurate calculation of excited state population dependence on local conditions difficult.

Two previous measurements of neutral xenon in gridded ion engine plumes have been performed using two-photon laser-induced fluorescence (2PLIF).[1,2] In both cases the signal to noise ratio and quantity of usable data was poor. No such measurement has been reported on a standard U.S. ion engine such as XIPS 13 or 25, NEXT, or NSTAR. While ion engines tend to have lower emission background than Hall thrusters, their xenon flux level is more than 10× lower at the exit. Another notable study utilized a movable rake of nude ion gages to directly measure far-field neutral xenon density.[3] Here the closest approach to the thruster exit plane was 50 cm. The nude ion gage is a simple, inexpensive alternative to the 2PLIF method, but it has poor resolution, perturbs the flow and cannot be used in the near field – at least not without considerable modification of the technique.

The xenon neutral measurements of the current study were performed on the SPT-140 thruster SN002 between 27 June and 11July 2012 at discharge voltage of 300V and either 3.0 kW (9.97A discharge current) or 4.5 kW (14.78A) power level. The nominal flow set points were about 100 and 140 sccm, respectively. In addition, extensive measurements were also made of the neutral flow field with thruster off and flow rate equivalent to the 4.5 kW set point. The test set-up and results are documented in this report.

II. Experimental Method

Two-Photon LIF

For two-photon absorption by xenon a rate equation expression can be written that is second order in the concentration of photons and linear in xenon concentration[4]

$$-\frac{1}{2}\frac{d[hv]}{dt} = k_2[hv]^2[Xe] \tag{1}$$

or equivalently

$$-dI = 2k_2c^{-2}I^2Ndx \tag{2}$$

Here I is the light intensity (photons/cm^2-s), c is speed of light, N is ground state concentration (atoms/cm^3) and k_2 is the rate coefficient (cm^6 sec^{-1} molecule^{-1} photon^{-1}). The constant $\delta = k_2/c^2$, known as the absorptivity, is essentially a cross section for two-photon absorption as σ is for one-photon absorption. However, the two-photon contribution to the cross section is given by 2δI, so that the cross section increases with light intensity. The value of δ for the xenon transition of the present study is on the order of 10^{-48} cm^4 sec/molecule-photon, but the precise value is unknown. With a laser intensity of 10^{25} photons/cm^2 sec, readily achieved during the present study, the absorption cross section for the second photon is of order 10^{-23} cm^2/molecule. This is very small for a one-photon process, but large enough to produce saturation under the measurement conditions.

Xenon Spectroscopy

Xenon atoms are relatively heavy, producing a narrow Doppler profile for a given temperature. The atomic weight is 131.29 g/mol for the natural isotopic abundance in Earth's atmosphere. There are 9 stable isotopes, atomic number 54, with abundances and nuclear spin as shown in Table 1. Both isotopic shifts in the center of gravity of the transition frequency and hyperfine splitting for some of the isotopes contribute to line broadening, however the hyperfine contribution typically dominates when present. For the upper state that was the subject of this study, we were unable to find an accurate measurement for isotope shifts or hyperfine splitting. Based on isotope shift and hyperfine studies of other Xe I transitions, the isotope shift here is probably small compared to the laser linewidth.

The manufacturer-specified linewidth is ≤ 0.04 cm^{-1} for the tunable dye laser fundamental frequency. The dye laser frequency can be obtained from

$$\nu_{dye} = \frac{1}{2}\nu_0 - \nu_{355}\ cm^{-1}\ , \tag{3}$$

where ν_{355} = 28191.5 cm^{-1} is the approximate frequency (in wavenumbers) of the tripled Nd:YAG laser and two photons are absorbed for each excitation event. The upper and lower energy levels for the xenon transition are separated by ν_0 = 89860.54 cm^{-1} (111.3 nm); therefore the dye laser has the approximate value 16738.8 cm^{-1} (no wavemeter measurements were made in this study).

For xenon atoms the full-width-half-maximum (FWHM) Doppler width is

$$\Delta\nu_D = \frac{\Delta v}{c}\nu_0 = \frac{2\sqrt{2R\ ln2}}{c}\sqrt{\frac{T}{M}}\nu_0 = 6.25 \times 10^{-8}\nu_0\sqrt{T} \tag{4}$$

if the velocity distribution is Maxwellian. In the above expressions R is the molar gas constant, c is the speed of light and M is the average atomic weight of xenon. At 298K the xenon Doppler width is 0.097 cm^{-1} for light absorption at ν_0. The equivalent width at the dye laser fundamental frequency would be 0.018 cm^{-1}, about half the manufacturer-specified laser linewidth. Assuming that the linewidth of the injection-seeded tripled YAG output is much less than the dye fundamental, the effective laser linewidth if the 0.04 cm^{-1} spec linewidth for the dye laser applies, is 0.08 cm^{-1} at ν_0. In practice, measurements of xenon lineshape are performed by scanning the dye laser fundamental frequency, reducing the magnitude of the "observed" value; every 0.1 cm^{-1} increment of the fundamental frequency corresponds to 0.2 cm^{-1} at the transition frequency.

The observed FWHM lineshapes corresponded to about 0.1 cm^{-1}, at minimum, at the dye laser frequency. Therefore, laser linewidth may be inadequate to explain the observation. Given the observation that 2PLIF signal is saturated with respect to laser intensity, power broadening must be considered. The magnitude of power broadening depends on the detection method, for example whether ions are being observed or fluorescence photons. If fluorescence photons are observed, as in the present study, the laser pulse duration relative to fluorescence lifetime is an important factor. Here the pulse duration is short compared to the lifetime. The study of another Xe I transition by Halfmann et al[5] showed that with laser intensity as high as 7500 MW/cm^2, 2PLIF broadening was small but multi-photon ionization broadening was very significant.

Table 1. Properties of the stable xenon isotopes

Property	*Xenon Isotope*								
	124	**126**	**128**	**129**	**130**	**131**	**132**	**134**	**135**
Mass (amu)	123.9059	125.9043	127.9035	128.9048	129.9035	130.9051	131.9041	133.9054	135.9072
Abundance (%)	0.10	0.09	1.91	26.4	4.1	21.2	26.9	10.4	8.9
Nuclear Spin, I	0+	0+	0+	1/2+	0+	3/2+	0+	0+	0+

Pressure broadening is, of course, negligible under SPT-140 operating conditions, but hyperfine splitting is another broadening mechanism to be considered. No studies on the upper state of interest were found, but considerable work has been done with high power, narrow bandwidth diode lasers on near infrared transitions between excited states, obtaining Doppler-free spectra that reveal isotope shifts and hyperfine structure. Isotope shift magnitudes relate to the change of nuclear radius with mass, whereas hyperfine splitting derives from the coupling between nuclear spin (I) and total angular momentum of the electrons (J). The magnitude of the splitting is very small - although somewhat larger than the isotope shift magnitude - because of the small magnetic moment produced by the nuclear spin. The total angular momentum of the atom is given by the sum

$$\boldsymbol{F} = \boldsymbol{J} + \boldsymbol{I} \tag{5}$$

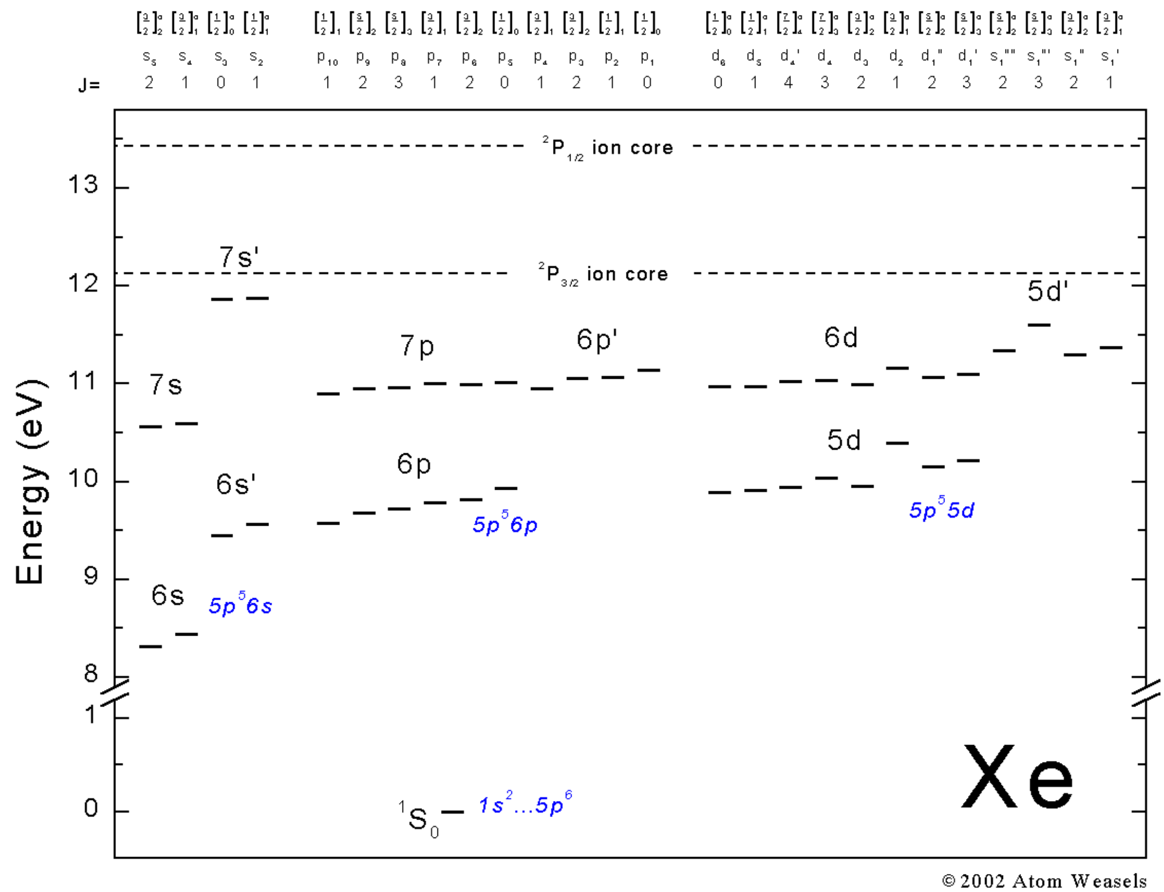

Figure 1. Energy level schematic for neutral xenon atoms (from http://raptor.physics.wisc.edu/data/data.htm).

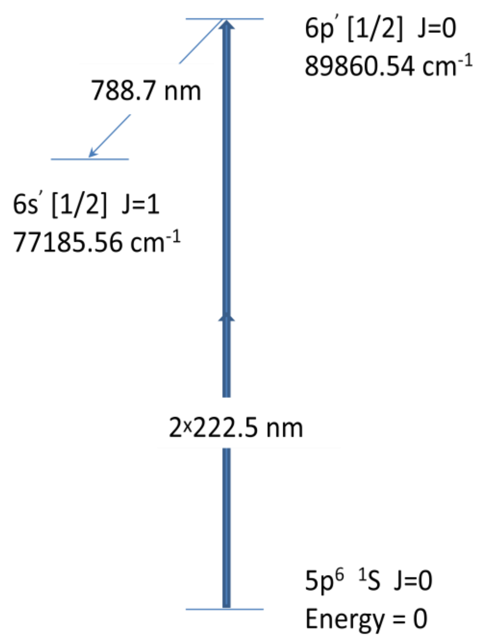

Figure 2. Two-photon excitation and detection scheme for neutral xenon atoms in the SPT-140 plume.

The quantum number F takes the values J+I, J+I-1, J+I-2, …|J-I|, with the number of hyperfine levels given by 2J+1 if J < I as it is here. But J = 0 for the upper and lower states of the transition, therefore the energy level is not split for upper or lower levels and there is no hyperfine structure regardless of the nuclear spin of the isotope. As a result the observed spectral width cannot be ascribed to hyperfine splitting either. The most likely explanation seems to be that the laser spectral linewidth was larger than expected. The laser linewidth could be determined with a suitable optical spectrum analyzer if such equipment were available. It could also be measured from the absorption spectrum of a reference gas, however this was beyond the scope of the project.

A diagram of xenon energy levels is given in Figure 1, showing that no excited states exist below 8 eV. There are three main manifolds of upper energy levels, based on which orbital the electron is in. Each manifold has 3 subgroups, and the individual levels in each subgroup are subject to isotope shifts and hyperfine splitting, depending on their specific quantum numbers. Transitions between levels are subject to selection rules.

The 2PLIF detection scheme for the present study is diagramed in Fig. 2, showing the specific levels connected by the 2-photon transition and the fluorescence pathway used for monitoring signal levels. Since fluorescence occurs at 788.7 nm, the detection system is relatively insensitive to room light, scattered photons at the uv wavelength, and even thruster emission background. The fluorescence pathway shown has a high branching ratio (0.62) and short lifetime (~38 ns).[6] This scheme may be preferable to the previous approach used at Aerospace[1,2] although a direct comparison has not been performed.

Laser Spectrometer

A Spectra Physics Pro270 injection-seeded Nd:YAG laser generated 532 nm and 355 nm pulses of ~370 and 100 mJ, respectively. The 532 nm photons were used to pump a Sirah dye laser operating on Rhodamine dye at 597.3 nm, as shown in Figure 3. The 597 and 355 nm beams were mixed in a BBO crystal to generate 222.5 nm uv pulses with output energy typically ~6 mJ. A Pellin Broca prism separated the 222.5-nm beam from the residuals. A quartz window on a flip mount was used to direct a fraction of the beam to a xenon reference cell for maximizing signal with respect to dye laser frequency. A series of four high reflector optics was used to direct the tunable uv beam to the vacuum chamber. These were coated for high reflectivity at 225-nm and 45-degree incidence.

A beam elevator raised the uv laser beam to the height of chamber centerline. A half waveplate (see Fig. 4-3) rotated the plane of polarization of the uv beam to produce minimum reflection at a Brewster window mounted on the chamber. A 2-m focal length lens placed ~2.3 m from the interaction region reduced the beam diameter to ~1 mm at the thruster, with the beam diverging as it crossed the axis of the fluorescence collection optic. The beam focus was placed significantly away from the monitoring region or region of interest (ROI) to avoid over-saturation and consequent signal reduction. A collimator made of a series of independently adjustable irises was positioned between the thruster and Brewster window to control scattered light levels around the beam. The laser beam and collection optic, a 6-inch diameter spherical mirror (see Figures 4 and 5), were aligned with respect to a fused silica window mounted at the top of the chamber, by suspending a plumb bob on a string running through the center of the mounting flange. The thruster “zero” position was obtained by running it forward on the positioning system until it just contacted the string. Side-to-side and up-down positioning was set by adjusting the motor-driven horizontal and vertical stage positions until the string and its laser-intersection point was visually centered on the thruster. The distance from thruster centerline to mirror center was set by adjusting mirror height to produce a converging beam that cleared the window aperture, producing a beam waist at the phototube for potential monitoring of Rayleigh scatter signal by one of us (E.J. Beiting), as shown in Figure 5, where the 45 degree filter reflects the Rayleigh scatter. This placed the mirror about 14 inches below the laser beam and about 82 inches from the focal point. Fluorescence at 790 nm passed through the long-pass optical filter and became divergent as it was directed to a lens (100-cm focal length, 1-inch Φ), which focused the light through a 790-nm bandpass filter (10 nm FWHM), circular aperture and smaller 1×5-mm slit to match the image of the uv laser beam as it crossed the region of interest (ROI). The long axis of the slit was aligned with the long axis of a phototube (Hamamatsu R636-10); misalignment of fluorescence image and slit axes may have produced some signal loss. The phototube detected fluorescence from the 6p’ excited state. This phototube has ~3× higher quantum efficiency and radiant sensitivity at the wavelength of interest (789 nm) than R955 tubes, lower dark count and a relatively small 3 × 12 mm viewing area. It was operated at three different cathode voltage settings: 900, 1200, and 1400V. The nominal gain ratio was estimated to be 7.6 for 1200 vs 900, and 3.1 for 1400 vs 1200, based on the manufacturer’s typical gain curve for phototubes of this type.

An energy detector (Coherent J3-09 pyroelectric) monitored the reflection from the Brewster window to provide a reference level proportional to the uv pulse energy. A beam attenuator with negligible beam direction shifting was used to evaluate the power dependence of the 2PLIF signal.

The BBO mixing crystal was angle tuned. Its temperature was not controlled, and thermal drifts proved to be capable of dramatic reduction of uv pulse energy. This occurred if the crystal was set at the angle for maximum uv production or on the high temperature side of the optimum, eventually causing a rapid rolloff of uv energy. With careful adjustment and stable room temperature, the uv output could often maintain itself at a nearly constant value for several hours without further adjustment. It was essential that the output be stable, since uv beam pointing was sensitive to any change in the crystal phase match conditions. Beam position drift at the thruster was amplified by the long lever arm.

Difficulties were encountered with burning of the coated uv high reflectors, particularly at the base of the beam elevator. Substitution of a fused silica right angle prism did not solve the issue, as it appeared to be forming color centers, and subsequent substitution of a uv-quality Pellin Broca prism was also not without issue. Although uv pulse energy was about 6 mJ approaching the base of the beam elevator, energy at the thruster was normally in the range of 2-3 mJ.

The spherical mirror, purchased from Edmund Optics with 30-cm focal length, was stripped and recoated in-house to achieve improved reflectivity at the uv wavelength. A grafoil-covered aluminum plate was swung by a rotary stage to cover or uncover the mirror. Its protection was necessary because the infrared laser measurements were done with thruster positioned about 16 inches away along the chamber axis, and the thruster beam would remove the mirror coating very quickly from this position without a protector.

High laboratory humidity (70-80%) was experienced day after day during the measurement campaign, resulting in significant chamber sweating in the vicinity of the fluorescence exit window, due to the proximity of four cryotubs. Eventually heating tape was wrapped around the flange, keeping its temperature well above the dew point but raising the phototube dark counts significantly and likely adding to the noise level.

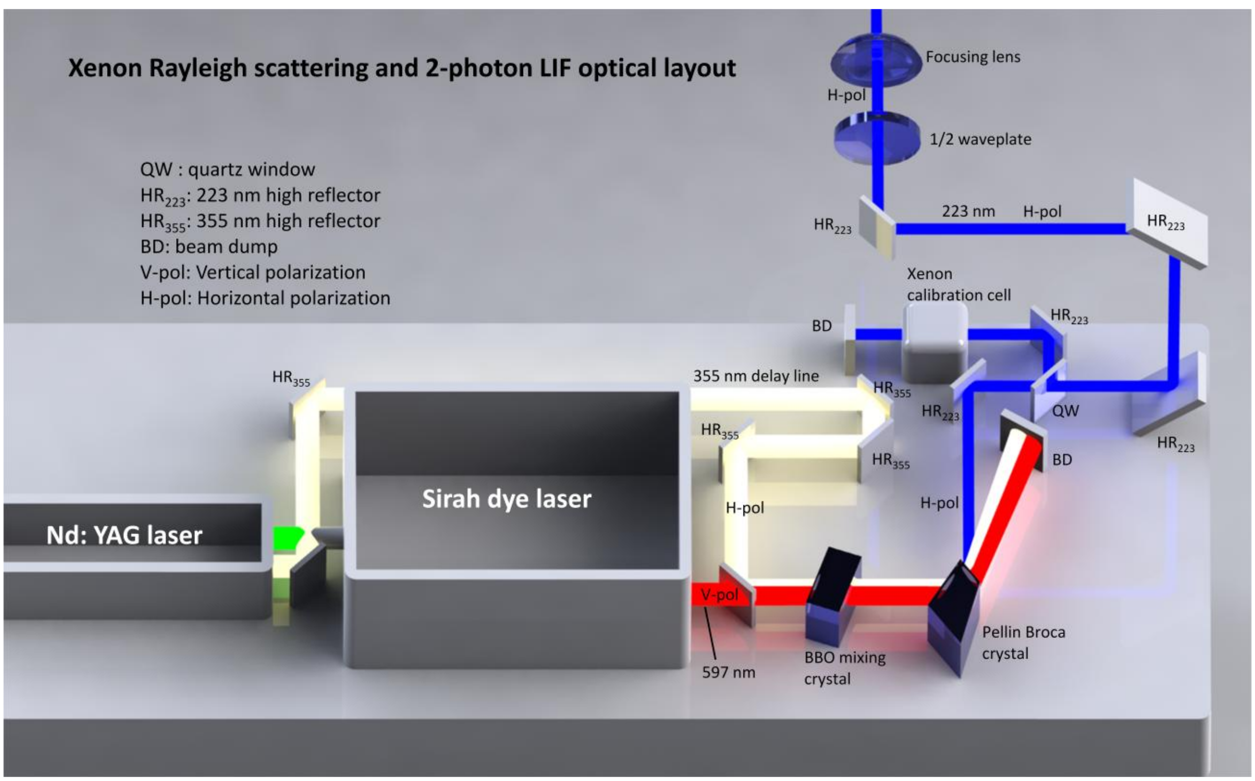

Figure 3. Diagram of the system for generating and manipulating the uv laser for 2PLIF.

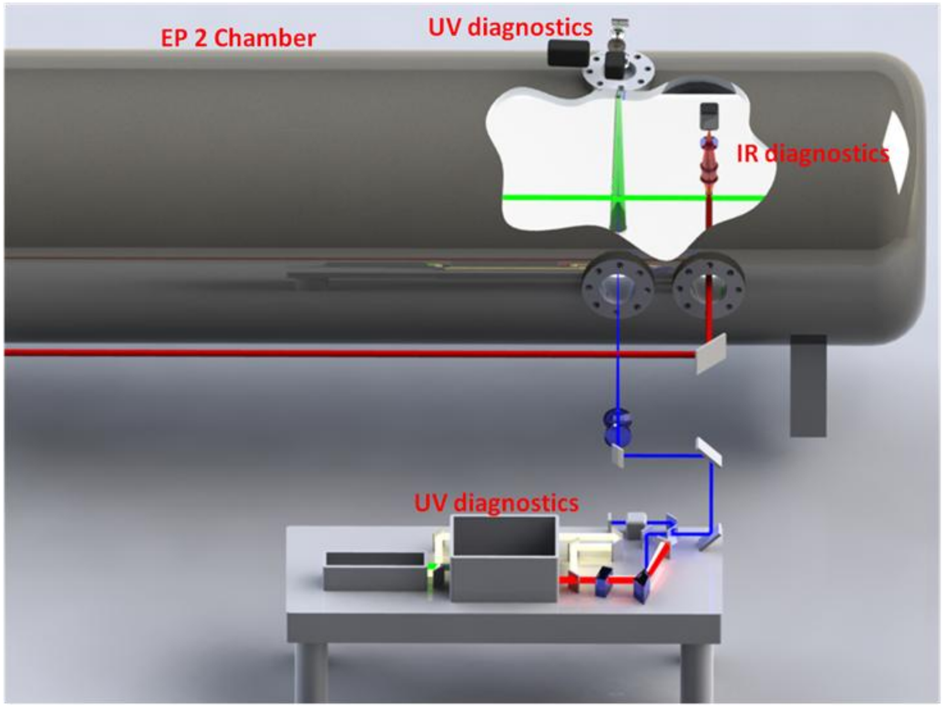

Figure 4. Overall diagram of the laser and detection systems, in relation to the test chamber.

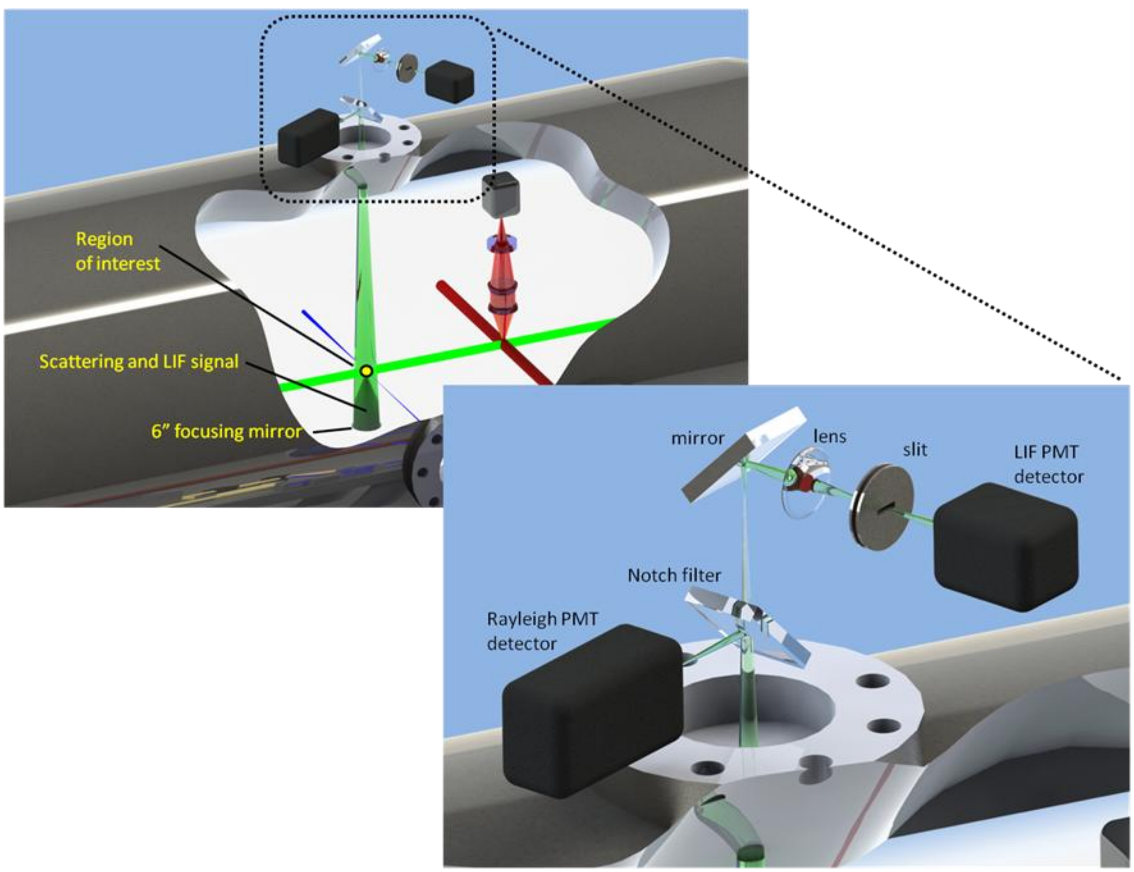

Figure 5. Detail schematic of fluorescence detection setup inside and above the test chamber.

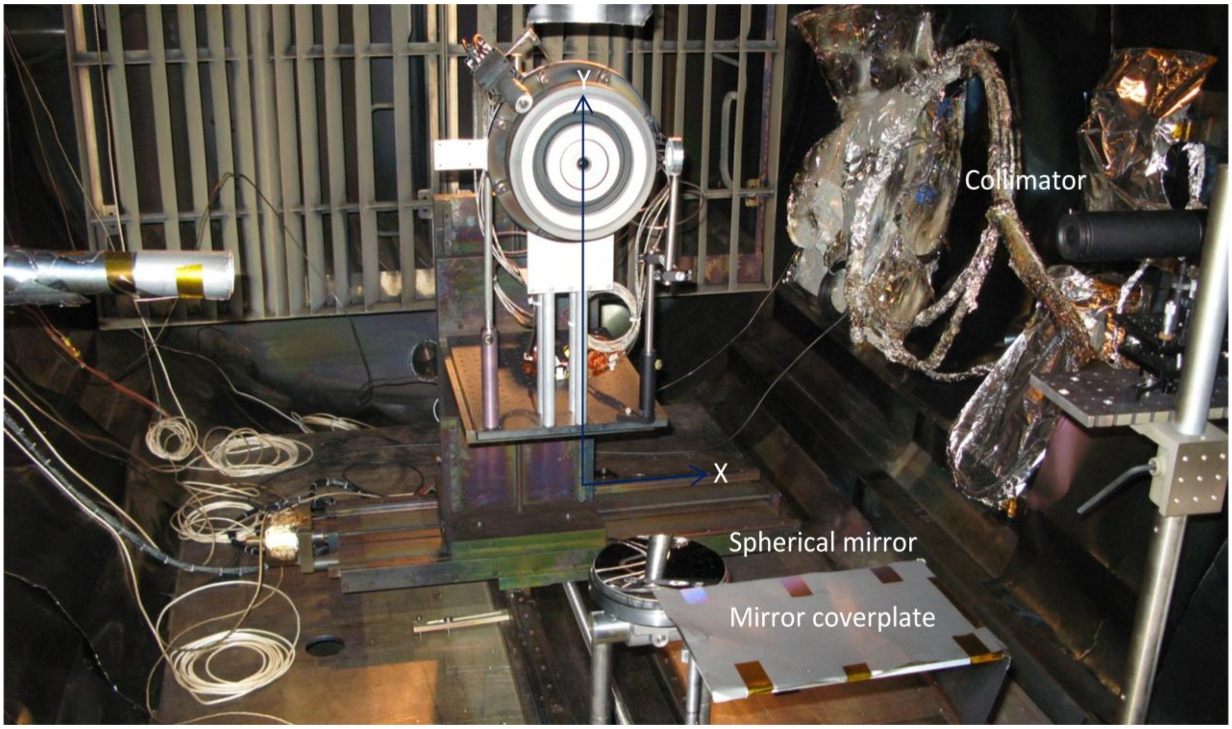

Figure 6. Photo of in-chamber setup.

Figures 6 and 7 show the in-chamber setup for laser measurements, which required the cathode to be located out of the path of incident and fluorescent light. The cathode was positioned at -45 degrees with respect to the nominal top location to achieve this. The thruster was cantilevered out from the positioning system to enable wide positioning system latitude without running into the mounting apparatus for the spherical mirror.

Signal Levels and Energy Dependence

As already discussed, saturation of the 2PLIF absorption was experienced. The dependence of signal on relative pulse energy was measured using a beam attenuator, which had an insertion loss of about 50%. The principal data set obtained is plotted in Figure 8, and indicates that significant signal drop did not occur until an overall energy reduction of 6× was realized (including the insertion loss). As a result, it was unnecessary to perform signal normalization during or between scans. Signal change due to drift in beam pointing was dominant over normal variations of pulse energy.

Data Acquisition & Processing

Stanford Research Systems boxcars (model no. 250) were used for gated detection of fluorescence signal, emission background, and relative pulse energy during 2PLIF measurements. Signal and background gate width was set for 40 ns, with 55 and 0 ns delays, respectively. Phototube, photon and cable propagation delays amounted to about 55 ns with respect to a photodiode trigger signal monitoring the dye laser beam on the optical table. A Canberra timing filter amplifier provided ×100 gain for the 2PLIF signal channel, and a second Canberra provided ×30 gain for the Molectron energy signal. DC signals corresponding to signal, background, and energy were acquired through a National Instruments USB-6210 data acquisition module and LabView program, on a shot to shot basis to allow normalization on a per pulse basis if needed. Because of the signal saturation this was not necessary.

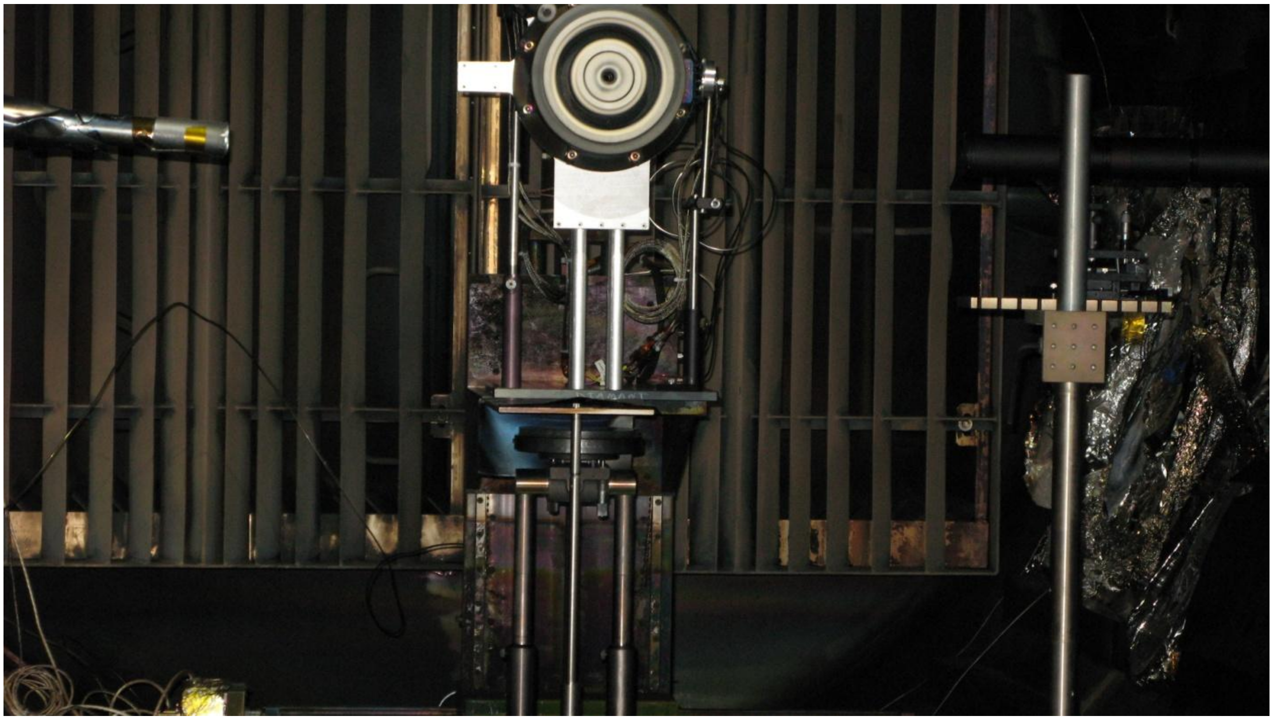

Figure 7. Photo of in-chamber setup, showing coverplate positioned over the spherical mirror.

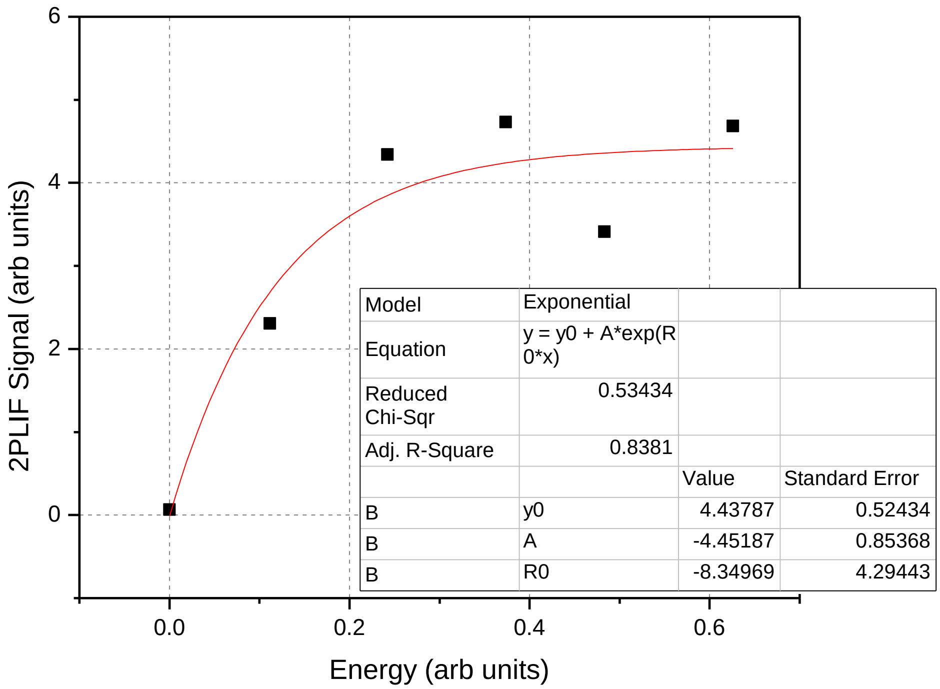

Figure 8. Measured signal dependence on uv pulse energy.

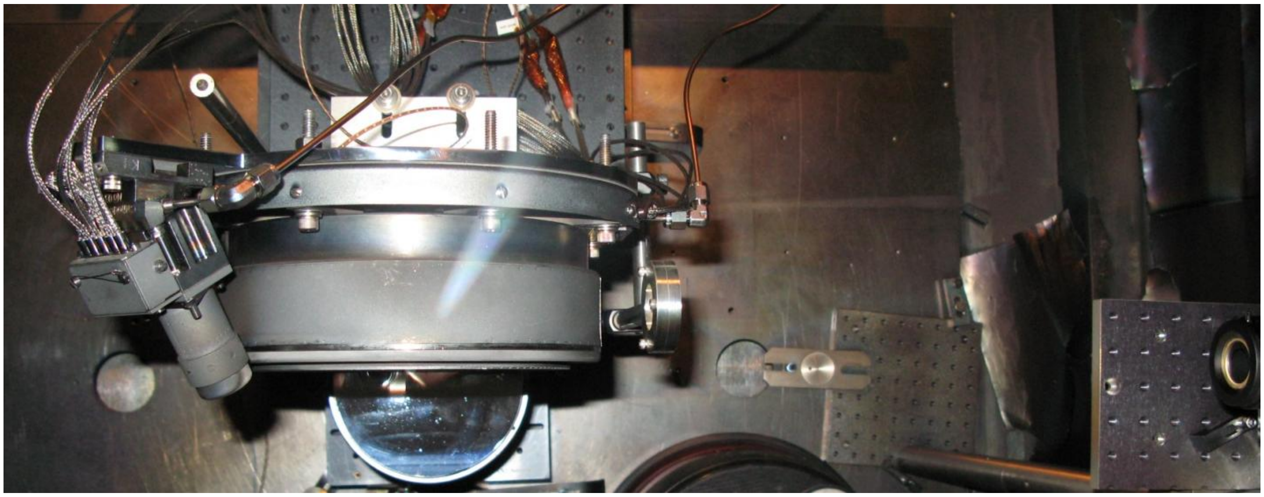

Figure 9. View looking down on SPT-140 thruster and mirror below. This mirror has the stripe mentioned in the text. A boron nitride disc was mounted to the side as a laser beam diagnostic.

Signal Correction for Occluded Mirror Effect

When the uv laser beam transits near the thruster exit plane, the amount of fluorescence collected by the mirror below and transmitted through the window on top depends on the thruster x, y and z coordinates. This effect is due primarily to blockage by the SPT-140 body of the light beam formed by the mirror, on its way to the window. Since the thruster body diameter is 8 inches and the mirror diameter is 6 inches, during X translation there is a section up to 14 inches wide during which blockage may occur. The length of this section depends on the z coordinate. If z is 3 inches, no blockage can occur except for the relatively small contribution from the cathode. The cathode can block at most ~1.1% of total mirror area (Figure 9 is relevant here), and its contribution was therefore ignored. The mirror generates a weakly converging beam and the dependence on y position is larger; it is estimated to be about 8% across the channels. Since the principal purpose of the y-scans was to obtain lineshapes and divergence figures, the y dependence was also neglected. Mirror area loss associated with thruster "shadowing" is illustrated by Figures 9 and 10. The calculated reduction of effective mirror area for a grid of x and z values is plotted in Fig. 4-11. The x-grid points were interpolated for a given z value to find correction factors for the coordinates of the data scans. The mirror convergence slightly reduces blockage and changes the effective z coordinate relative to the plotted curves. To address this issue, an effective z coordinate was used for normalizing signal levels during x and z data scans, obtained by multiplying z by a scaling factor of 0.89. Correction curves on a 0.25-inch grid with respect to z coordinate were obtained by averaging corrections for nearest neighbors on the 0.5-inch grid. Data were corrected by choosing the closest correction curve from the 0.25-inch grid.

Coordinate System and Measurement Locations

As described in other sections of this report, a 3-axis positioner with right-handed coordinate system was used to place the thruster at various locations with respect to the interaction region (the region where 2PLIF measurement was occurring). Figure 12 illustrates the geometry (all dimensions were hand-measured, and may deviate slightly from actual; e.g. the outer channel diameter may be 140 mm rather than 138.2 mm as implied by the measurement). Measurements were taken along a horizontal span up to ~51 cm travel (x axis), and along vertical cuts up to 18.3 cm in length (y axis). The z axis coincided with the thrust axis, and axial scans were performed over distances of about 40 cm. The latter scans were limited in time duration and length by mirror deterioration that occurred when the thruster was positioned at a large axial distance from the mirror. Numerous y-scans were performed for various fixed x coordinates and numerous x-scans were performed for various fixed y coordinates. For the latter with $y \neq 0$, the scan length was typically shortened to reduce scan time while covering the entire region involving the thruster.

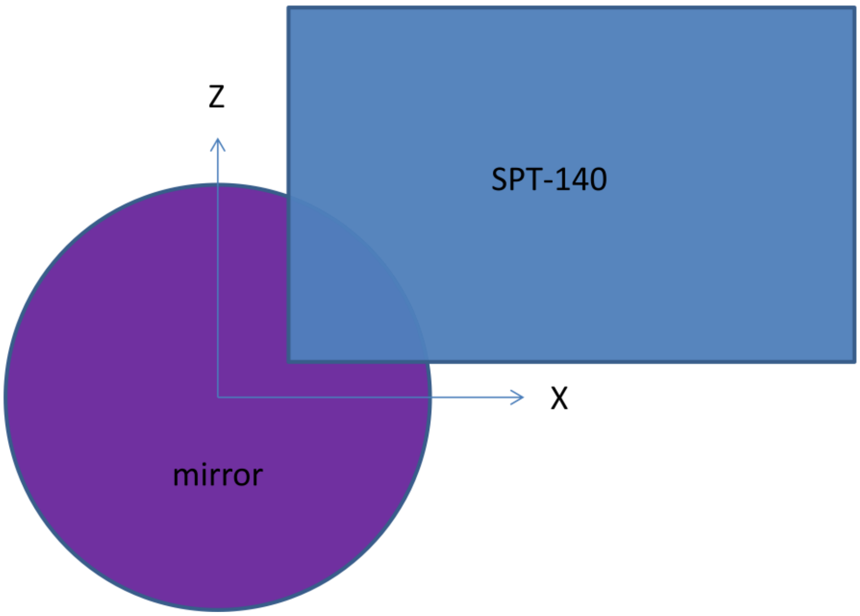

Figure 10. Illustration of mirror occlusion caused by the overhanging thruster, resulting in reduced fluorescence signal at the detector. The view is down, along the y axis. Coordinates of the SPT-140 corner nearest the mirror center are x=5.00, z=0.50 (x=4.00, z=0.00 when the corner is at mirror center). The mirror loss factor for this case is 0.11 (no "stripe" in this case and y-factor neglected).

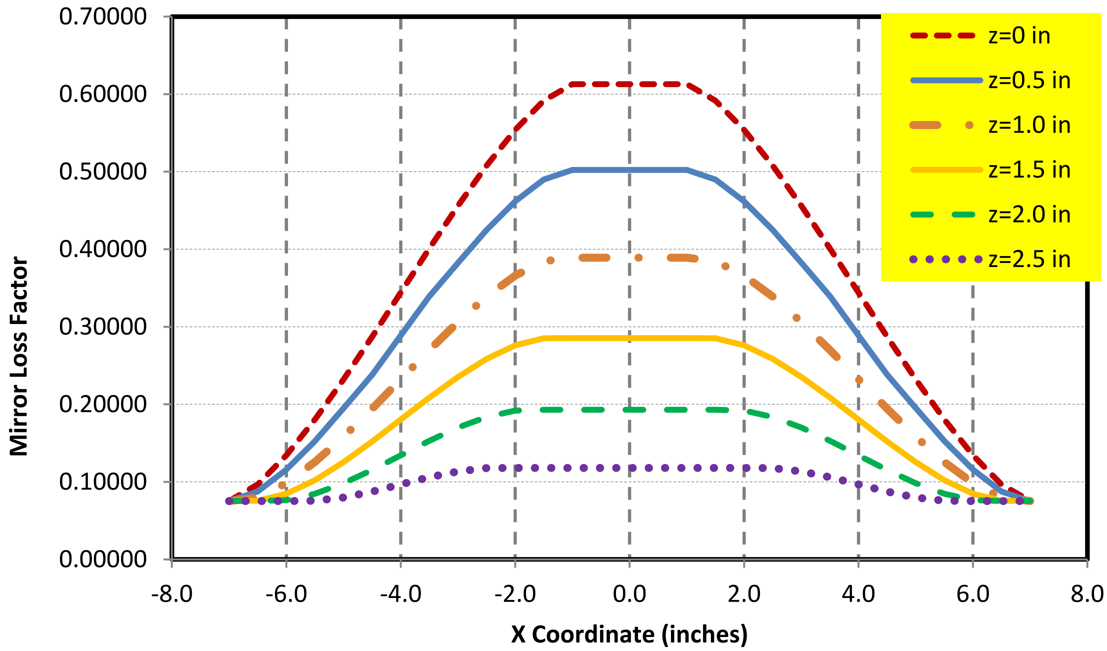

Figure 11. Calculated mirror loss factor associated with overhanging thruster, including the ~7% loss associated with a 0.75-inch stripe along one edge. Positioning system coordinates are as shown.

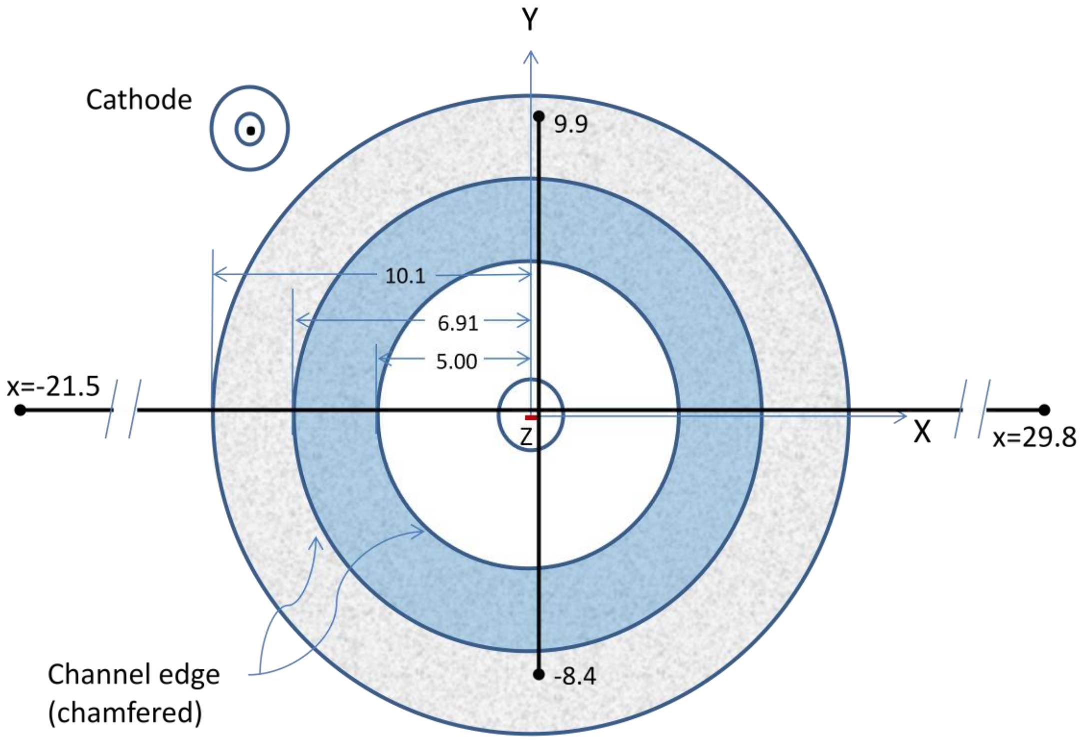

Figure 12. Right-handed coordinate system for the measurements, showing range of motion and thruster geometry. Positioning system displacements are always specified in English units, but in the diagram all dimensions are in centimeters. The cathode is canted toward the thrust axis (not shown). The short red line corresponds to the laser probe region, which is fixed in space. When x=29.8 cm, the laser probe region or region of interest (ROI) is 29.8 cm to the left of thruster centerpoint (on same side as cathode). At x,y = 8.4, -8.4 cm the cathode position approximately coincides with the ROI.

III. Xenon Neutral Cold Flow Measurements

Cold Flow Results

Xenon flow through the non-operating thruster is simplest to measure and mathematically model. Signal levels were far above those observed when the thruster was in operation. Figure 13 presents the density obtained by scanning horizontally on the thruster mid-line. High flux through the channels is apparent, peaking on their centers (±6.0 cm). An obvious asymmetry exists between cathode and anti-cathode sides of the thruster, with roughly 40% higher integrated flux on the anti-cathode side and a slightly broadened peak on the cathode side. This may have to do with the way the xenon flow is channeled through the anode. A further asymmetry exists for the baseline on either side (density ~3× higher for the anti-cathode side at x= -20), as shown in Figure 14. Noticeable deviation begins at x = -10 or -11, where the density profile on the anti-cathode side has a more gradual slope. Possible explanations for the latter observations include collisional scattering out of the annular flow. Evidence for this includes x = 0 density that is more than an order of magnitude above facility background.

Figure 15 is concerned with determination of baseline density. Signal decreases slowly between x = 15 and x = 30, the limit of the positioning system for the configuration of the test. The baseline is obtained by taking the moving average and linear trendline extrapolations to x = 30. By assuming that value corresponds to the background pressure of 4.0×10^{11} cm^{-3} measured by the wall-mounted Stabil-ion gage mounted closest to the thruster, absolute density as displayed in Fig. 13 was obtained. To check the accuracy of this assumption, the quantity $\frac{1}{4}vn(r)2\pi r dr$ was numerically integrated over the -15 to +15 cm portion of the scan, using the measured density profile (averaging across the horizontal cut and otherwise assuming annular symmetry). The result was total flux equal to 6.0×10^{19} atoms/s.

Total flux in atoms/s for a 140 sccm flow rate can be obtained by converting units, with result equal to 6.3×10^{19} atoms/s, quite close to the integrated value obtained from the data. The atom density at the exit plane is related to total particle flux via the relation

$$F = n v_e A_e = \frac{1}{2} n \sqrt{\frac{8kT}{\pi m}} A_e \qquad (6)$$

Here A_e is exit area of the annulus, n is the neutral density at the exit plane of the thruster, v_e is the average axial velocity of the escaping neutrals (equals $\frac{\bar{c}}{2}$), T is the neutral temperature and m is the atomic mass. The expression $(8kT/\pi m)^{1/2}$ gives $\bar{c}$, the mean 3-dimensional speed of xenon atoms. Solving for n yields 8.0×10^{13} cm^{-3}, which is approximately the average peak density for the plot in Figure 16. However, the measurement is performed slightly downstream and the channel exit is rounded, also there may be significant scattering and divergence effects. So the peak density near the exit plane can be greater than the calculated average across the channel, and the width of the profile broadened beyond channel width.

A collection of horizontal scans (x-scans) at various axial distances from the exit plane is plotted in Figure 16.

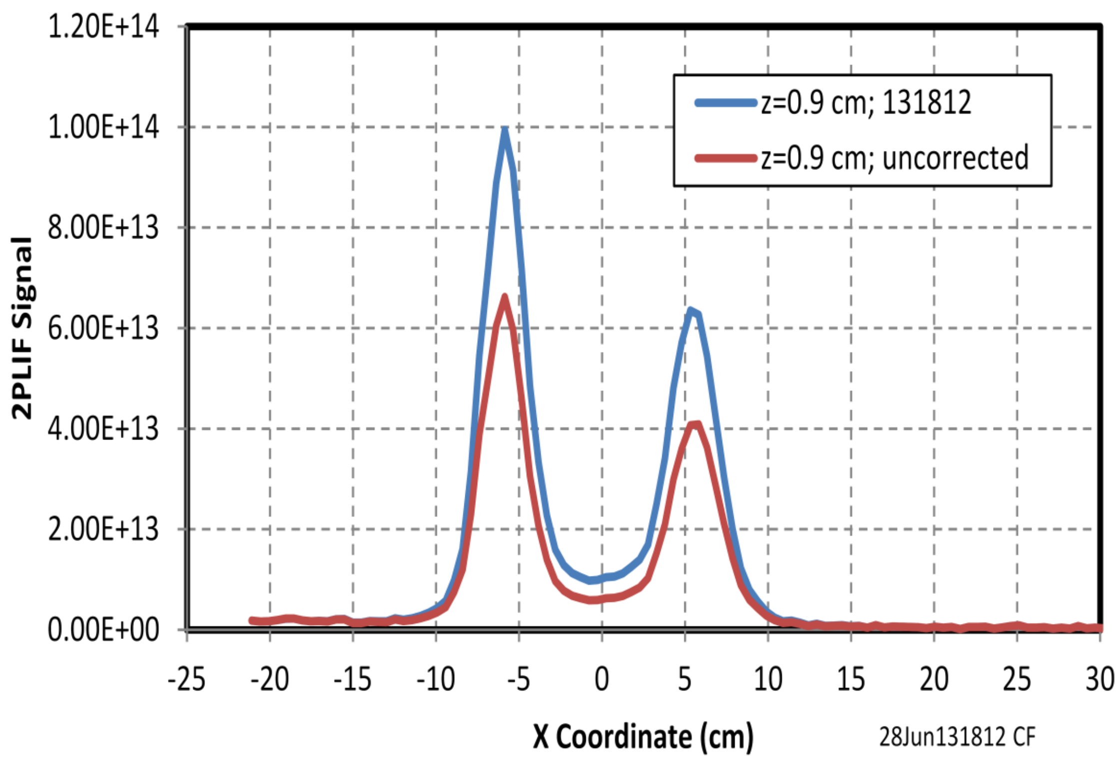

Figure 13. Measured cold flow density across the thruster face and slightly downstream with ~140 sccm flow rate through the SPT-140 anode. The plots are identical, except that the mirror loss factor was not applied to the "uncorrected" plot. An obvious asymmetry exists. Positive x values correspond to the cathode side.

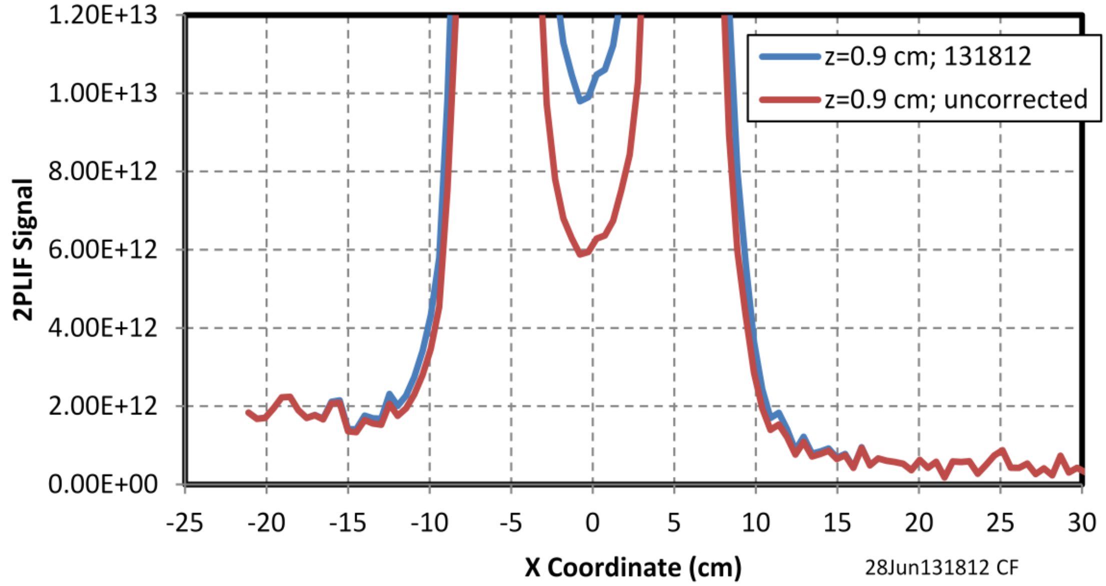

Figure 14. Figure 13 with modified scale, showing baseline divergence on opposite sides of x=0, for extreme values of x.

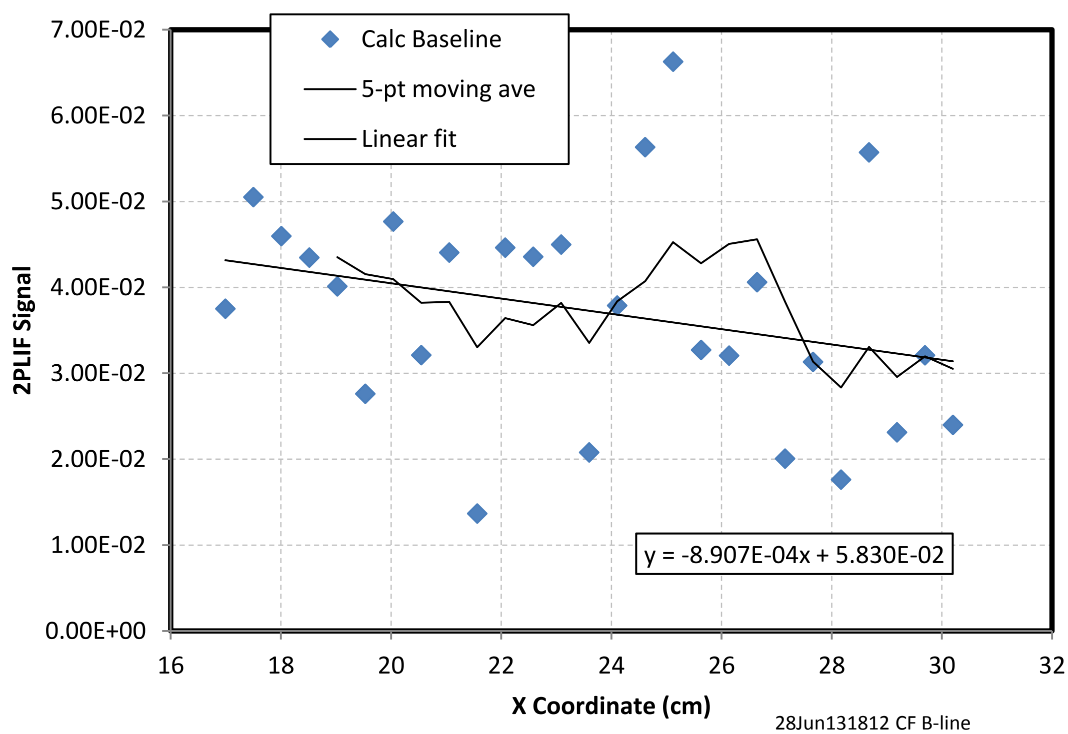

Figure 15. Determination of baseline signal corresponding to background pressure.

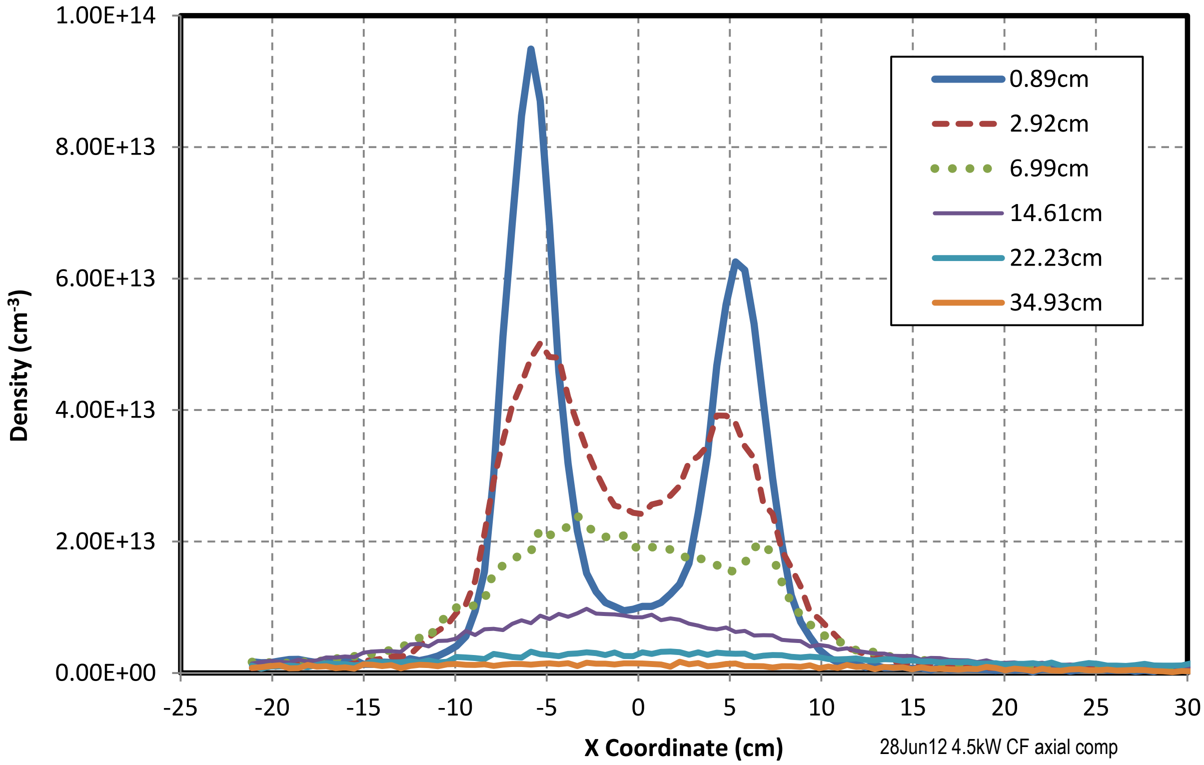

Figure 16. Series of horizontal scans at various axial distances, for the ~140 sccm cold flow condition.

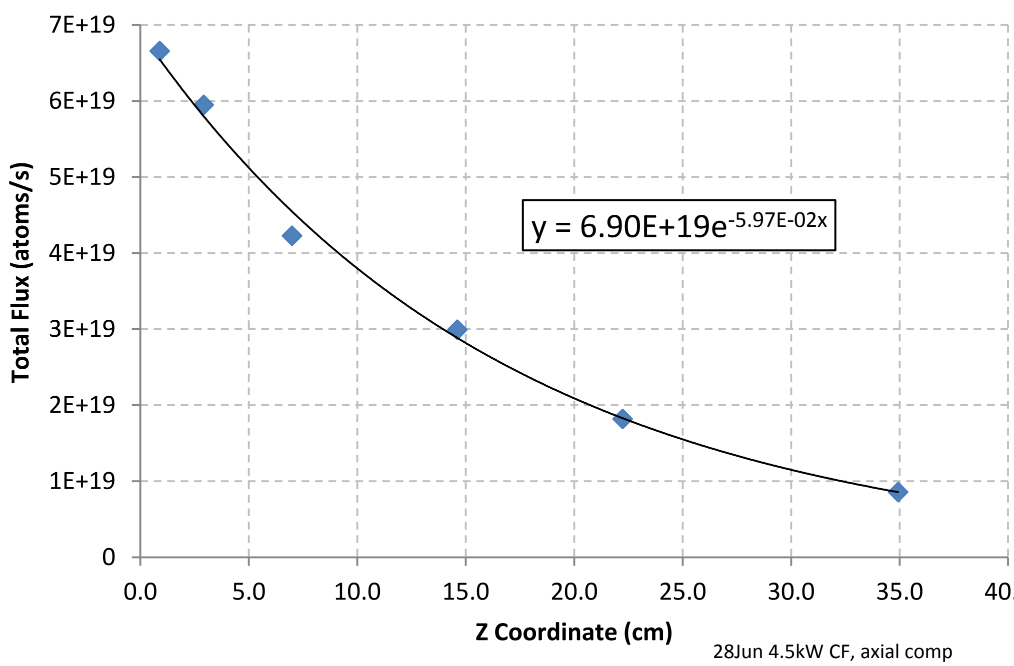

Figure 17. Dependence of integrated flux on axial (z) coordinate, over the x coordinate scan range of -21.5 to +29.8 cm.

There is a general trend of higher density on the anti-cathode side. When z is large, there is still a noticeable density difference between opposite sides, both at opposing channel locations and for extreme x values. The integrated flux over the scan range of the x coordinate varies for this data set as shown in Figure 17. It decreases exponentially as the plume broadens with distance from the exit plane and more atoms are located outside the scan range. Pulse energy and therefore beam pointing was more variable for data obtained at z =7cm, which probably accounts for the anomalous deviation there from the exponential trend.

A series of vertical scans, cutting across the thruster face at z = 0.9 cm, is plotted in Figure 18. Each scan produces two peaks, unless performed near x = ±6.0 cm (here the scan passes through the center of the annulus). The final scan of the series, at x = 5.72 cm, approaches this value. The peak positions would be expected at the midpoint crossing of the channel at positive and negative y coordinates of the same magnitude, with $y = \pm\sqrt{R^2 - x^2}$, where R is the radius of the annular center (center of the channel). Each scan was fit to a dual Gaussian peak function, and the results are given in Table 2. An example fit for the case x = 4.80cm is given in Fig. 4-19, and the behavior of peak positions and widths is shown graphically in Figure 20. Based on the plots, there is good peak position symmetry with respect to y=0, and peak widths steadily increase with axial distance. Symmetry with respect to x=0 is not as good.

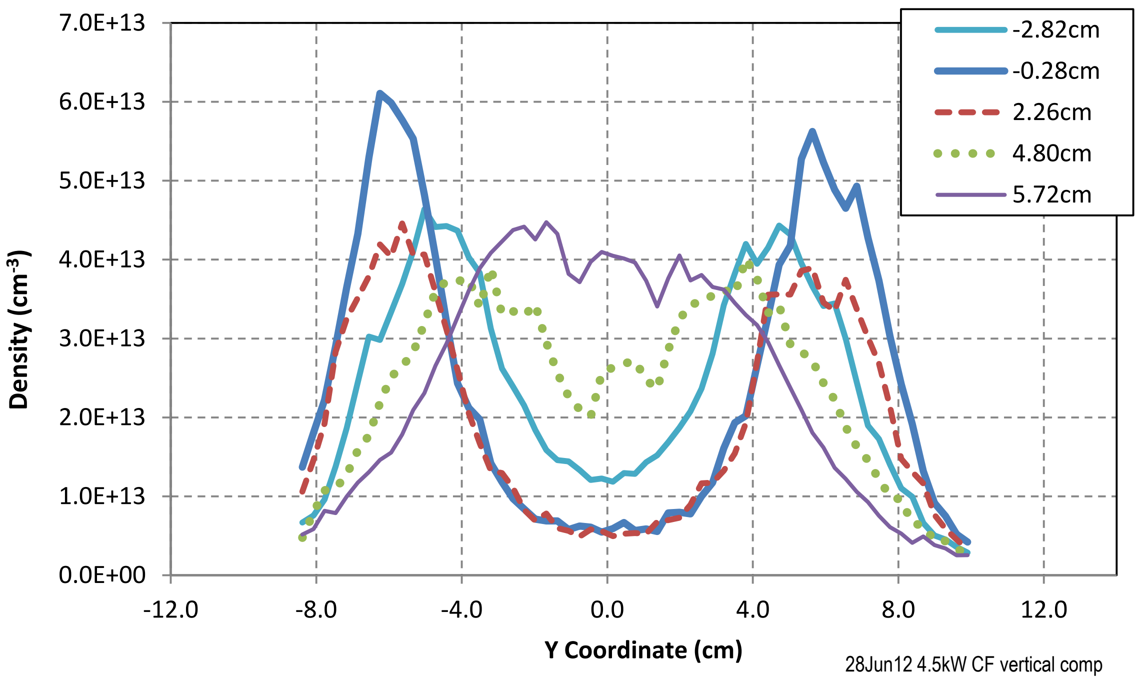

Figure 18. Series of y-coordinate scans at various x values (z is constant at 0.9 cm). The y coordinate for intersecting the annular edge varies with x.

Table 2. 4.5 kW peak fit results (28Jun) for cold flow y-axis scans with z = 0.89 cm and various X values. The data are plotted in Figure 18. A Gaussian profile was assumed, with 2 peaks for each scan and fit equation $n=n_0+(A/w)(2/\pi)^{1/2}\exp(-2((y-y_c)/w)^2)$.

Parameter	Filename				Standard Error			
	180259	**182439**	**184108**	**190441**	**180259**	**182439**	**184108**	**190441**
X (cm)	-0.28	2.26	4.80	5.72	-0.28	2.26	4.80	5.72
Center (y_1)	5.989	5.720	3.590	3.04	0.030	0.042	0.073	0.15
Width (Δy_1)	2.934	3.22	5.05	4.43	0.072	0.11	0.20	0.20
Area1	1.76E14	1.40E14	2.24E14	1.68E14	4.9E12	5.7E12	1.3E13	1.3E13
Center (y_2)	-5.861	-5.76	-3.804	-2.37	0.025	0.038	0.075	0.13
Width (Δy_2)	2.526	3.03	4.56	4.89	0.059	0.095	0.15	0.18
Area2	1.687E14	1.47E14	2.04E14	2.35E14	4.3E12	5.3E12	9.9E12	1.2E13

Axial dependence of the cold flow density, starting from near channel center at thruster bottom (x=-6.2cm, y= -0.13cm), is plotted in Figure 21. Line profiles obtained toward the start and end dates of project data collection are plotted in Figures 22a and b, respectively, together with fit results. These profiles are the same to within experimental error.

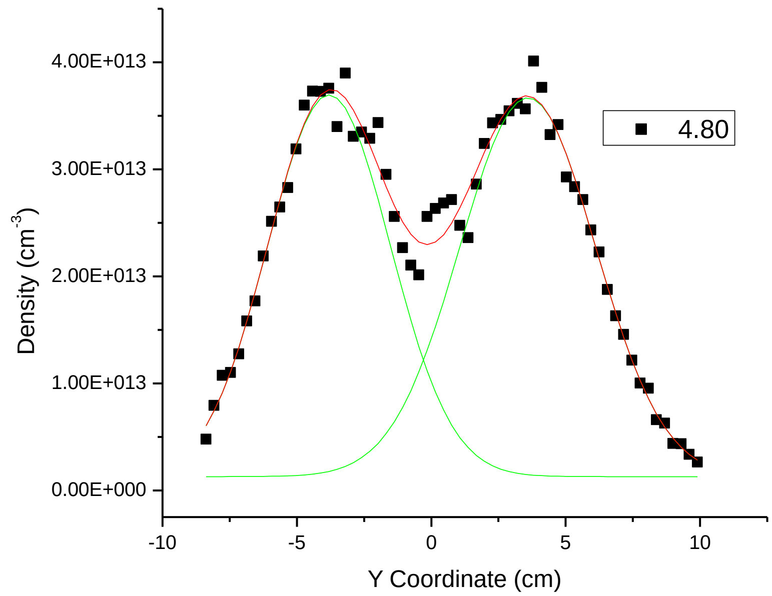

Figure 19. Example fit for x=4.80 cm data in Fig. 18. The red line is a composite of the individual Gaussian peakshapes (green lines) obtained by the fit.

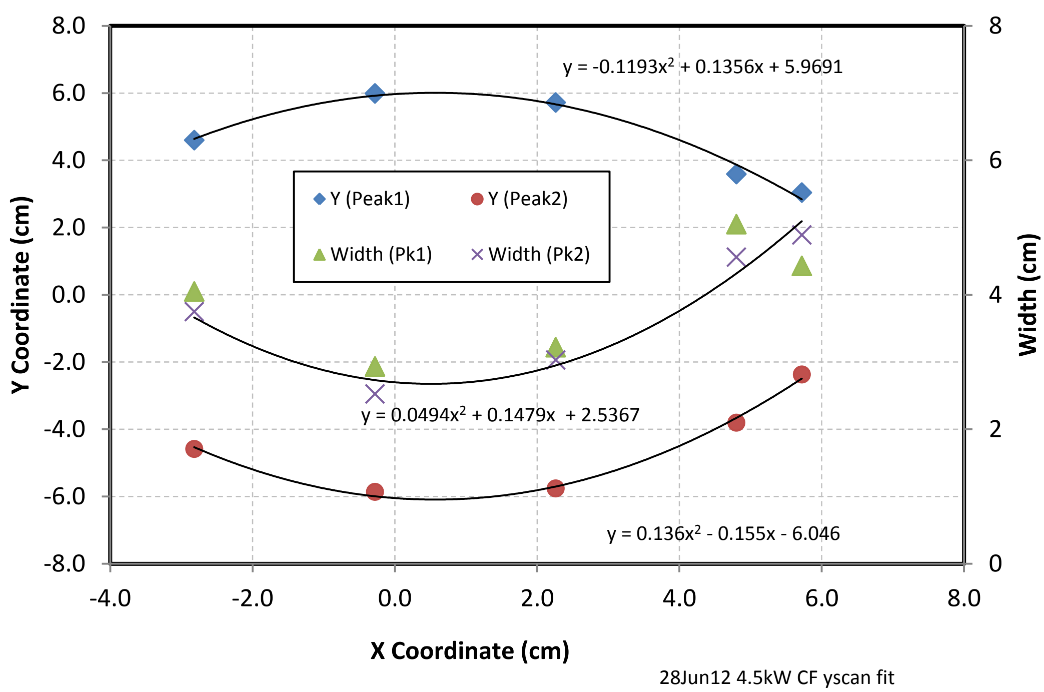

Figure 20. Plots of peak positions and widths for y-scan cold flow data, as a function of x coordinate. The fit for peak1 series width is not shown.

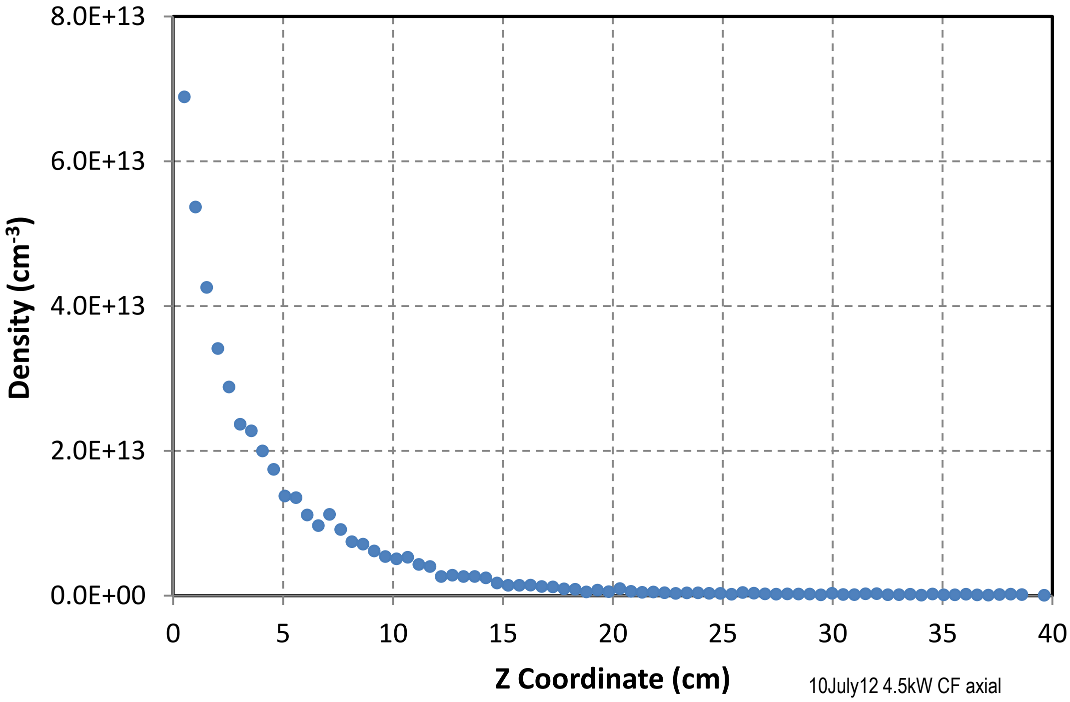

Figure 21. Axial density variation for approximately mid-channel scan (x= -6.2cm, y= -0.13cm).

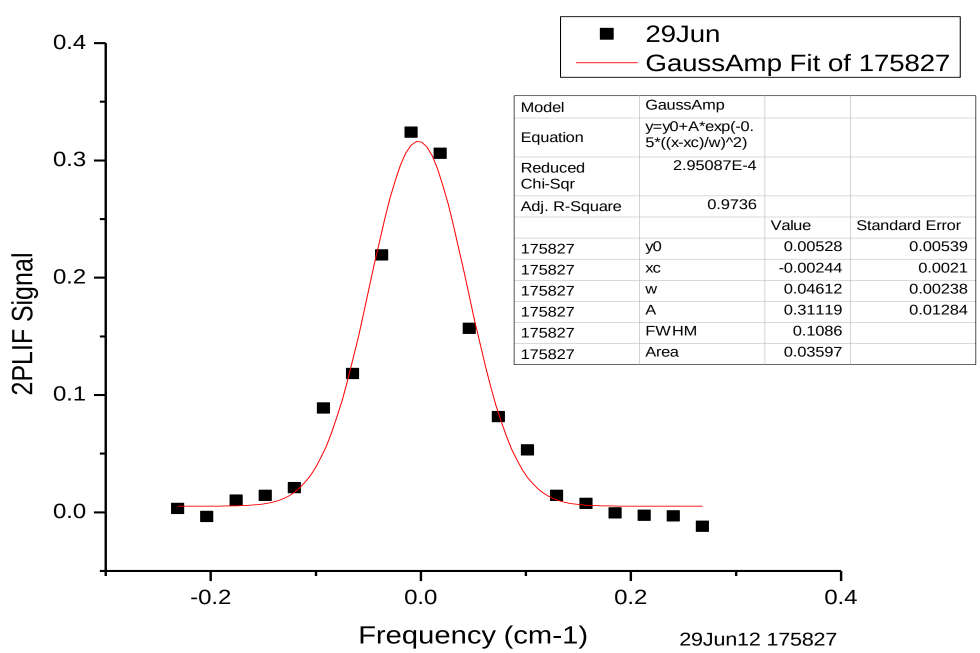

Figure 22a. Lineshape for cold xenon neutrals, with xenon bleed into chamber (no thruster flow).

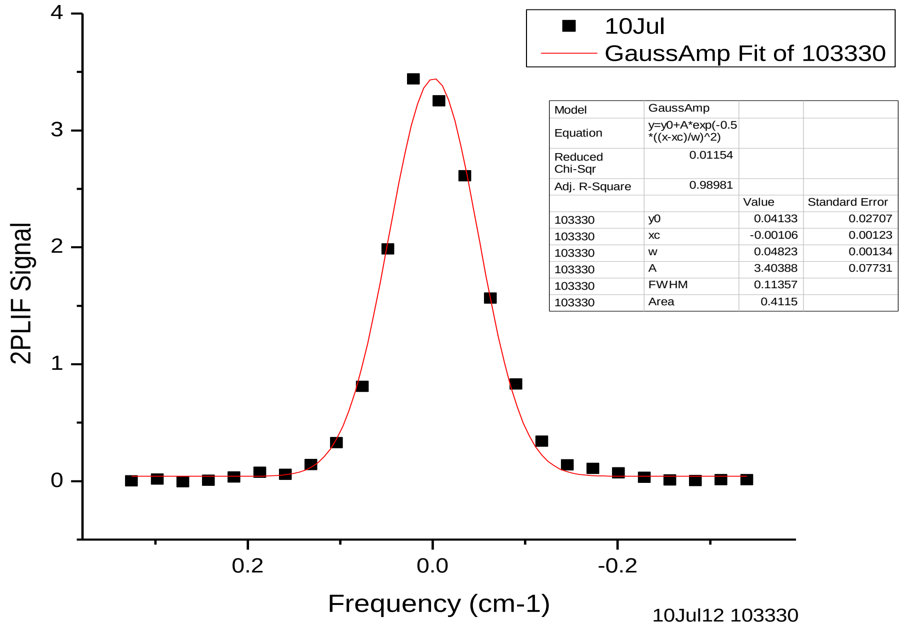

Figure 22b. Lineshape for cold xenon neutrals, with xenon bleed into chamber (no thruster flow).

IV. Xenon Neutral 4.5-kW Hot Flow Measurements

The result of a horizontal scan across the thruster mid-line at 0.8 cm axial distance and 4.5 kW hot flow operating point is shown in Figure 23, for data as recorded (uncorrected case) and data corrected for the fluorescence mirror collection function. Since mirror occlusion is largest when LIF is performed on centerline, density determination there will be lower than actual if based on the uncorrected profile. The corrected profile has a flatter baseline, and more prominent peaks at each edge of the annulus. A scaled, corrected density plot is given in Figure 24. The density at the mid-annulus dip is below the average background density in the vacuum chamber. The average density for the span between outer annular edges at the exit plane was about 90 times higher for a similar measurement under cold flow conditions, indicating as expected that the discharge is highly effective in lowering neutral density. The elevated exit velocity during thruster operation is, of course, partly responsible for lowering the density. The population of excited levels near the exit plane, associated with elevated electron temperature, could also play a role – no correction for this has been attempted. The presence of neutral density maxima associated with the channel edges is not completely unanticipated; one numerical simulation of a "6-kW laboratory thruster" is consistent with that feature. But the simulation results presented in Fig.4 of that study[10] are at variance with respect to the divergence angle and sharp mid-annular density minimum found here for the SPT-140, as well as the axial persistence of the density elevation.

A lineshape fit of the four most prominent peaks in Figure 24 is plotted in Fig. 25. A Gaussian peak shape was assumed; the sharp dips at the annular mid-point naturally cannot be reproduced.

The horizontal scan across the thruster mid-line shown in Figure 26 exhibits the highest signal to noise ratio obtained for any hot flow case, except for measurements made near the cathode tip. The axial coordinate was near the lower limit; due to the finite width of the laser beam and its slightly non-parallel traversal, 2-mm was the practical lower limit (here Z was 3 mm). The peaks are labeled according to their identification with inner and outer sides of the annulus. The large amplitude difference between adjacent peak pairs is associated with laser frequency; the neutrals are emerging with elevated velocity and divergence angle that changes sign for inner and outer peaks on opposite sides of the channel. Divergence characteristics are illustrated by Figure 27, and the photo in Figure 28 shows the complex geometry of the inner and outer channel edges near the exit plane.

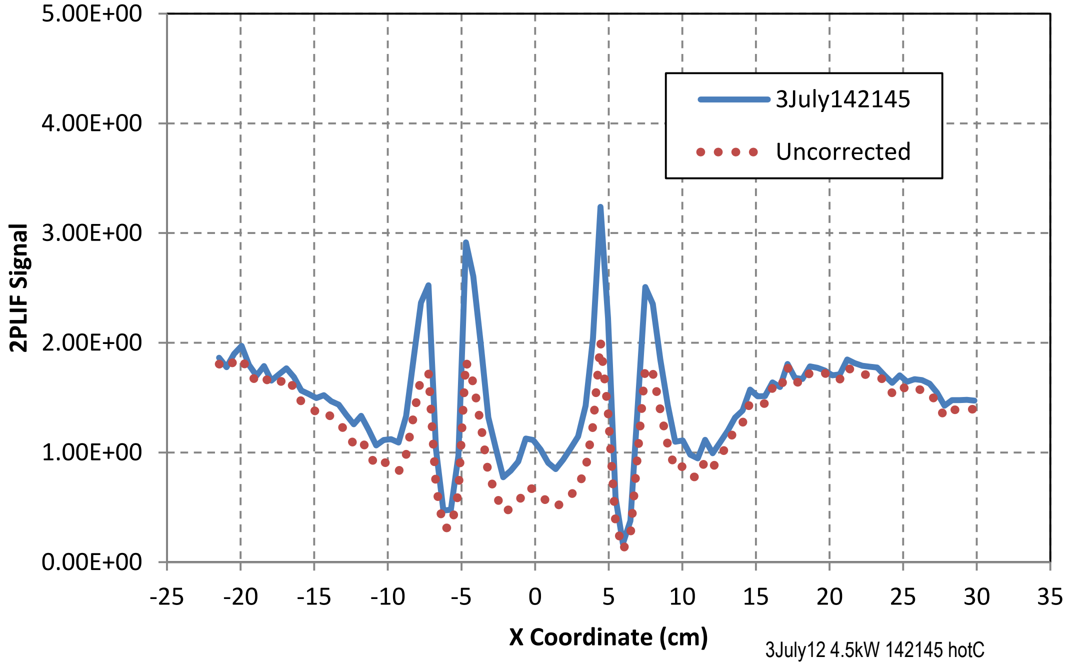

Figure 23. Horizontal mid-line scan at the 4.5 kW operating point, Z=0.8cm, showing the neutral jet fingerprint at annular edges.

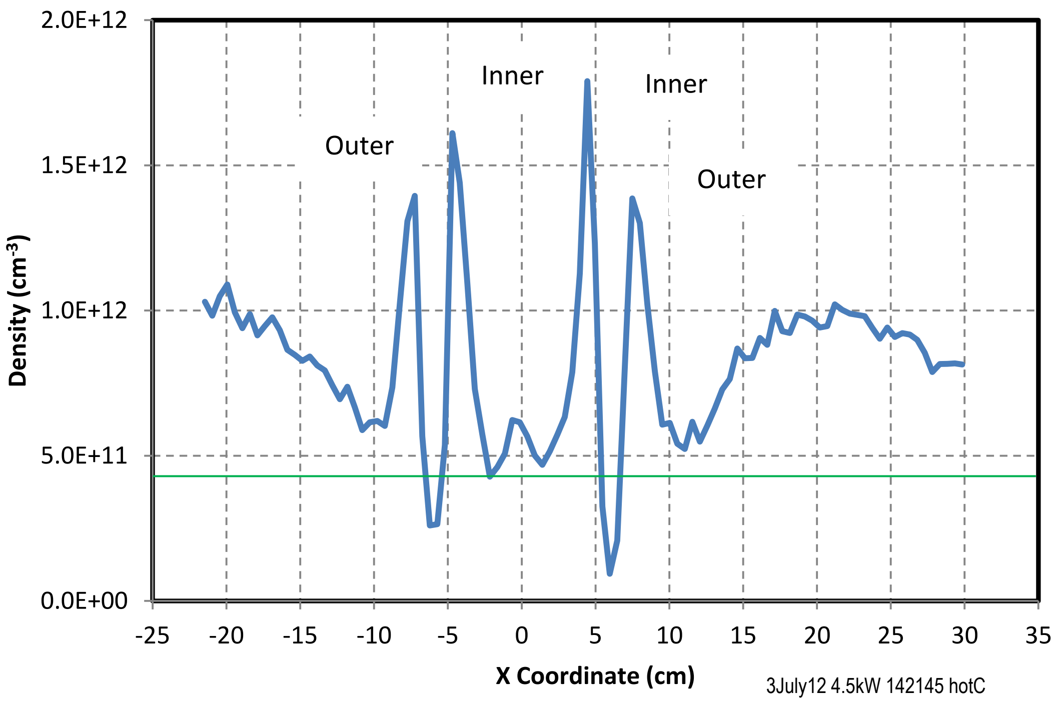

Figure 24. 4.5 kW corrected data for horizontal mid-line scan, Z=0.8cm, converted to density. The green line indicates background neutral density at the facility wall.

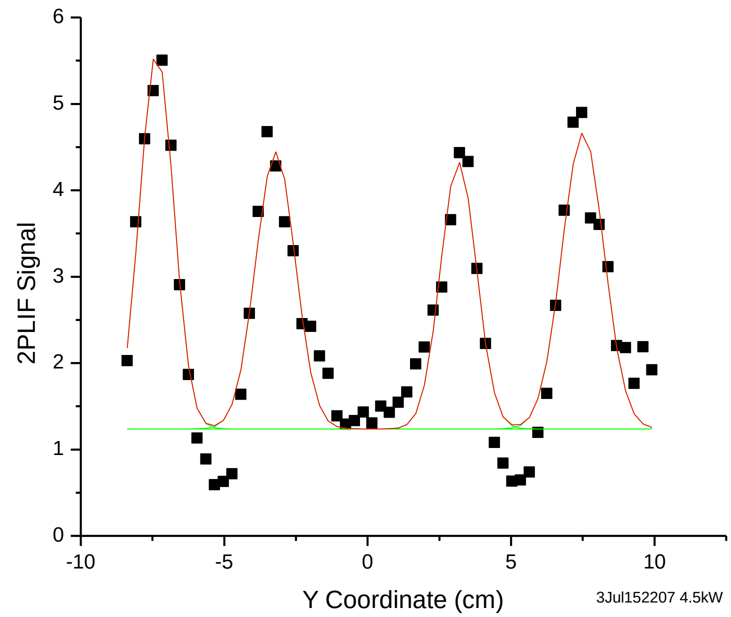

Figure 25. Gaussian peak fits for vertical scan with Z=1.0cm, X=-2.82cm; 4.5 kW operating point. The fits cannot reproduce the dramatic dip of neutral density in the center of the channel, or the in-board shoulders near Y=0.

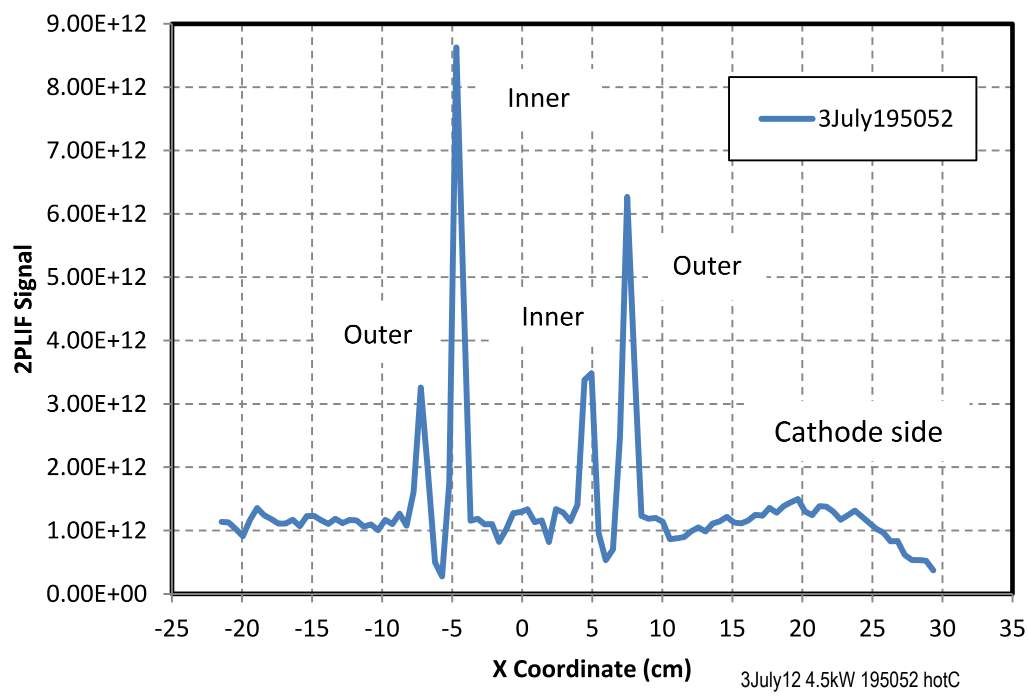

Figure 26. Horizontal scan on thruster mid-line at 4.5 kW operating point, with laser frequency matched to jet neutrals having a velocity component in the direction of the laser beam.

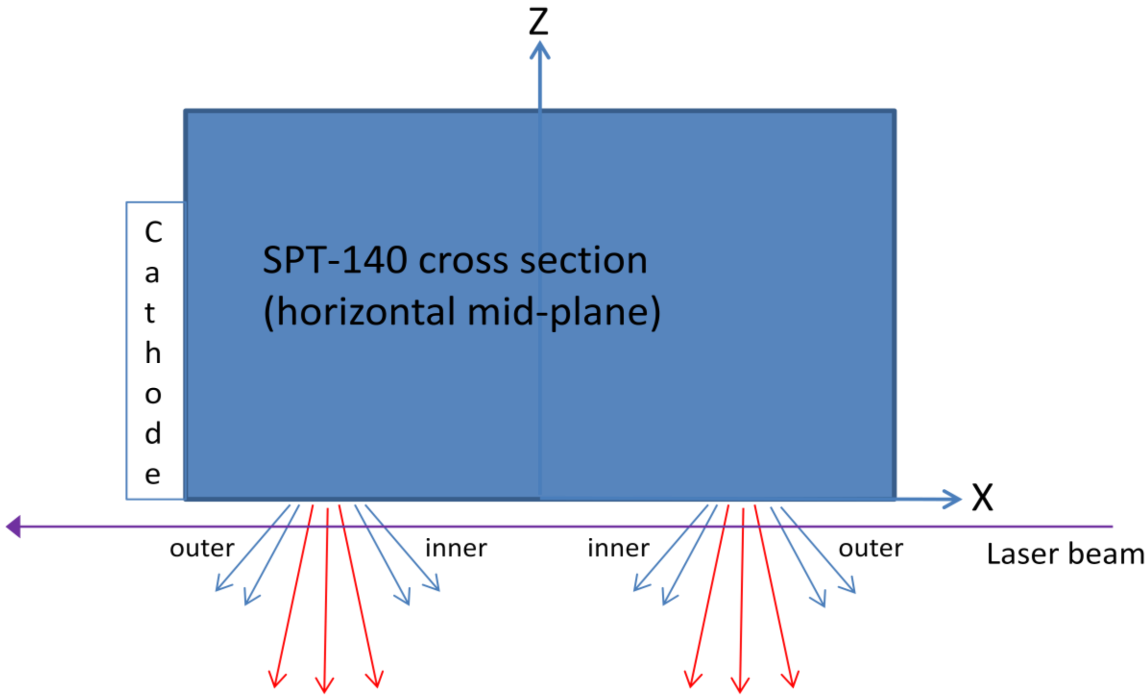

Figure 27. Streamlines for exiting neutrals and ions, shown with blue and red arrows, respectively. Cathode cant is not shown. Neutrals exiting according to the red streamlines would exhibit little Doppler shift with respect to the incoming laser beam; neutral flux along the thrust axis is low, as shown by the data. Some ions are believed to exit with trajectories similar to the blue arrows, and neutrals with red arrow type trajectories.

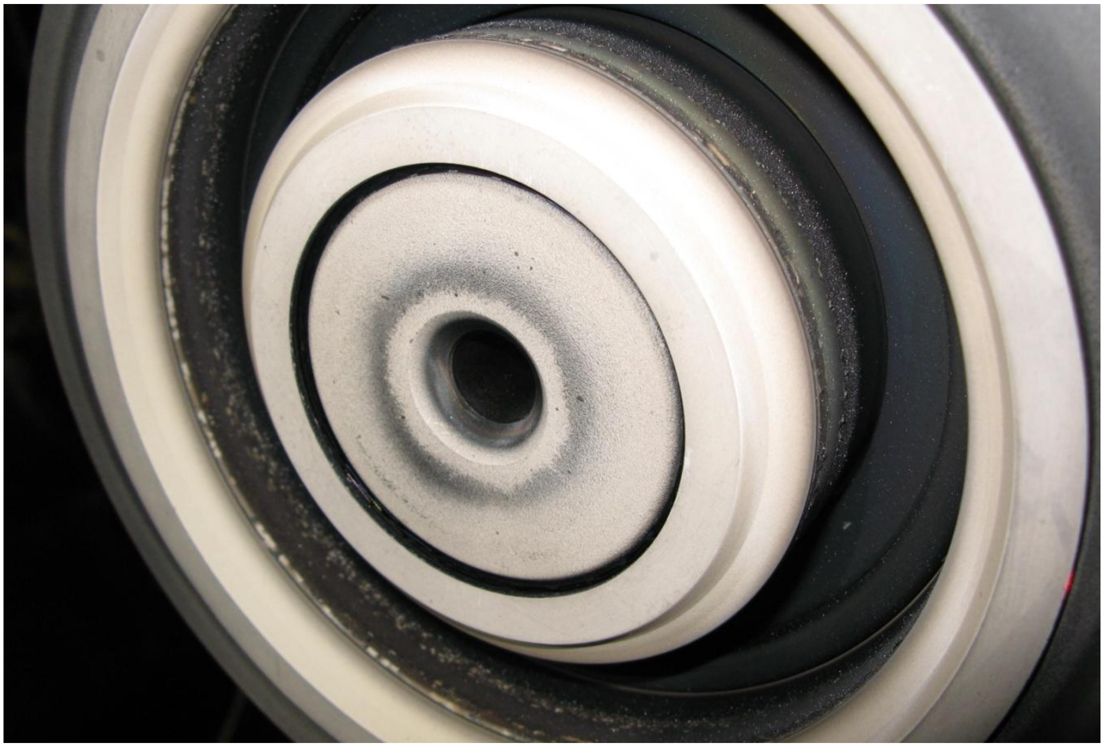

Figure 28. Photograph of SPT-140 thruster showing geometry of the channel exit and anode surface. The aperture on centerline is open through the back of the thruster.

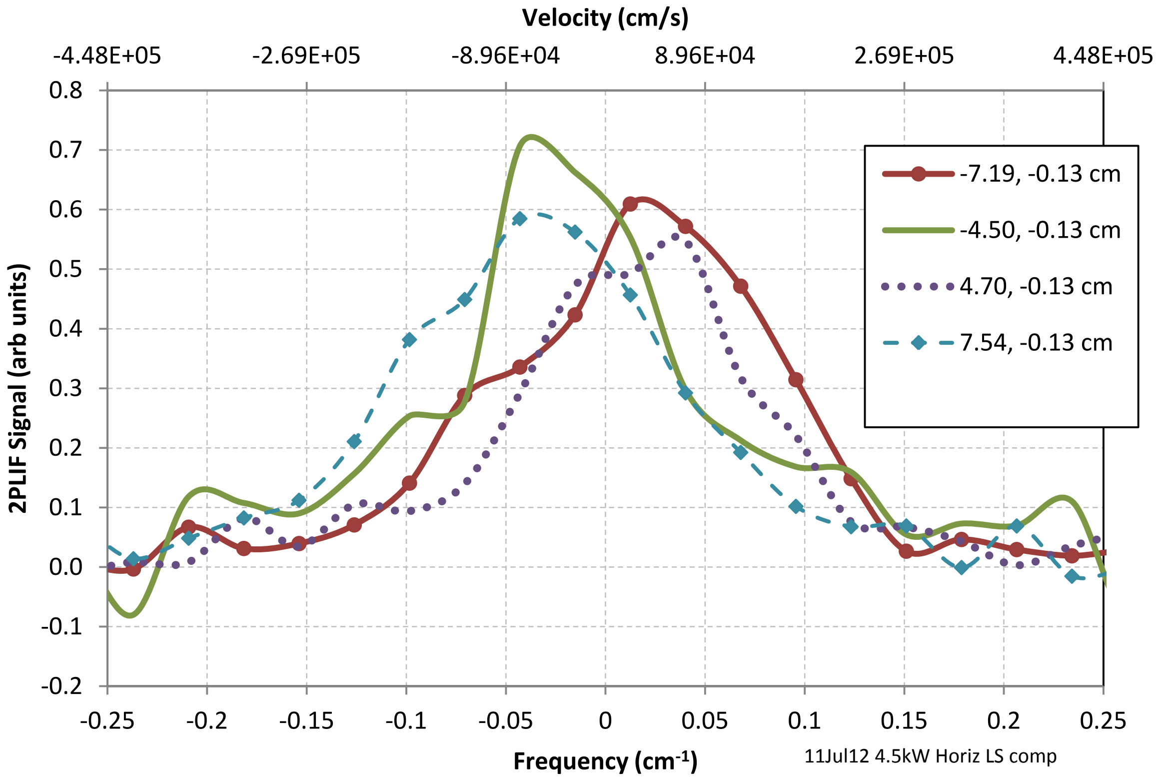

Figure 29. Recorded laser scan profiles at various x coordinates (-7.19, -4.50, 4.70 and 7.54 cm) and fixed y,z = -0.13, 0.15 cm, demonstrating the Doppler shifts of emerging xenon atoms. The x coordinates approximately match the inner and outer edge locations of the annulus. Gaussian fit results are given in Table 3. No spectral deconvolution, or velocity correction for different neutral beam and laser beam directions, was performed.

Lineshape scan data at various x coordinates are plotted in Figure 29. The Doppler shift associated with velocity component along the x coordinate is large enough that the laser frequency can coincide simultaneously with only two peaks rather than all four. That this is the case becomes more apparent when the Gaussian fit profiles for all four lineshapes are plotted together as in Figure 30. If the laser frequency is positioned at the peak position for two of the profiles, it is near a half-maximum point for the other two profiles. The parameters derived from the Gaussian lineshape fits are given in Table 3. These were used to generate the plots in Figure 30 where, as always, negative frequency corresponds to a Doppler red shift and positive to blue shift.

The lineshape profiles were plotted against both wavenumber and velocity in Figure 29 for convenient comparison, but it is important to note that the laser linewidth and xenon Doppler profile have not been deconvolved. The velocity axis therefore should only be used to assess the Doppler shift of the peak positions.

A series of thruster midline scans along the x coordinate at various axial distances is plotted in Figure 31. The sharp peaks seen in scans closest to the exit plane are due to the neutral jets emerging at the inner and outer annular edges and continuing to propagate downstream. The neutral jet profiles broaden quickly with axial distance and shift with respect to x. A mid-annulus dip is apparent for the smaller axial distances, and a very broad, shallow dip may be present even at z=7.0 cm. Asymmetry in the peak shape is apparent in some of the scans, due to sharp tail offs of the profiles on the mid-annulus side. Neutral density is higher on the anti-cathode side for the scan closest to the exit plane, as observed in cold flow results (compare to Figures 13 and 16). Scans at larger axial distances may deviate from this trend, and have increasing rather than decreasing density at large x values on the cathode side. However, density on the anti-cathode side drops monotonically with axial distance whereas it increases on the cathode side to become the region of highest density across the scan profile, with values well above facility background and peak position appearing to trend with increasing axial distance toward increasing x values. For the larger axial distances cathode-side density is clearly higher than density on the other side. The reason for this accumulation of neutral density on the cathode side at large x is uncertain. While the cathode produces the highest region of neutral density in the plume, its contribution falls very quickly with distance from the cathode exit plane. Perhaps these neutrals were emitted obliquely from the cathode, and the lower density at smaller x values is caused by higher ionization rate there. Another explanation that may be more likely is related to gas transport in the facility and surface collisions near the interrogation region (see discussion on this topic later in the report).

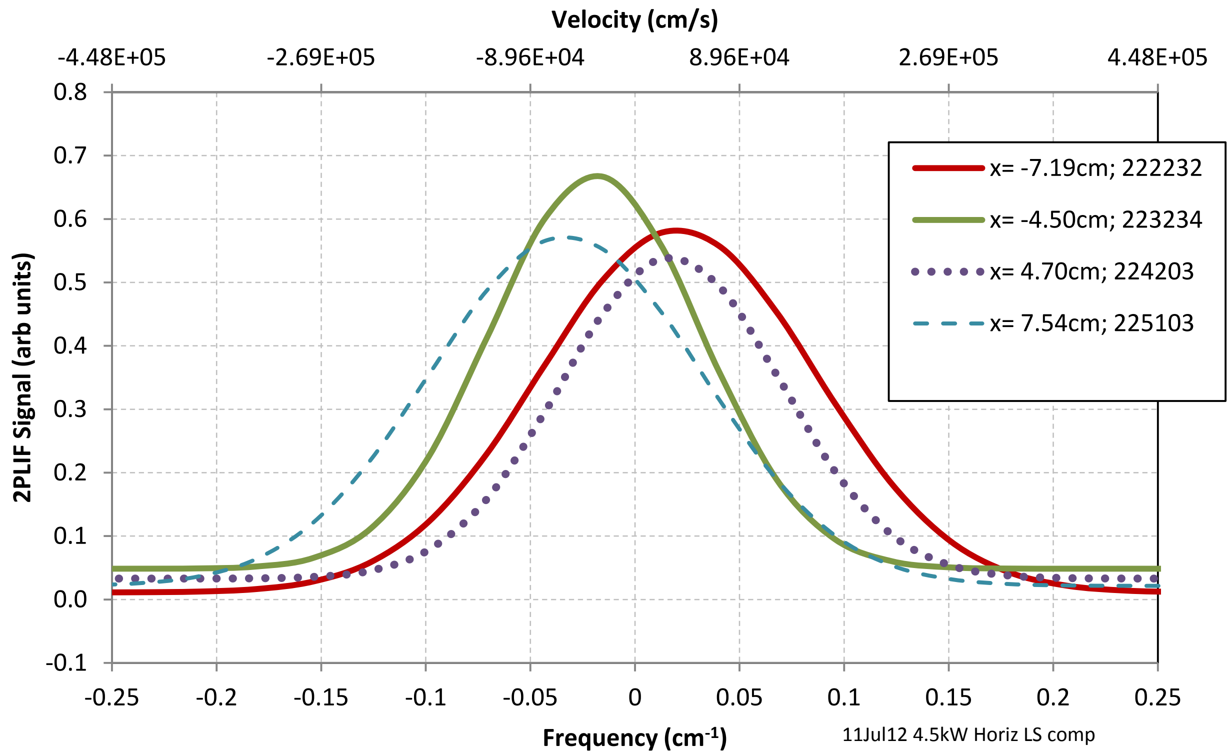

Figure 30. Fitted lineshapes based on Figure 29 and Table 3 results.

Table 3. 4.5 kW x-axis lineshape fit results 11Jul for y = -0.13 cm, z = 0.15 cm and various x values, obtained by scanning laser frequency. The fit equation was y=y0+A*exp(-0.5((ν-ν$_0$)/w)^2). Data are plotted in Figure 29 and fit results in Figure 30.

Parameter	Filename				Std Err	Std Err	Std Err	Std Err
	222232	224203	223234	225103	222232	224203	223234	225103
X (cm) =	-7.19	4.70	-4.50	7.54	-7.19	4.70	-4.50	7.54
Baseline (y0) =	0.0076	0.0330	0.0485	0.0216	0.011	0.0105	0.019	0.0073
Center ($ν_0$) =	0.0205	0.0174	-0.0189	-0.0330	0.0031	0.0033	0.0048	0.0021
Width (w) =	0.0659	0.0528	0.0503	0.0654	0.0036	0.0036	0.0053	0.0024
A =	0.571	0.506	0.620	0.550	0.025	0.028	0.053	0.0162
FWHM (Δν) =	0.155	0.124	0.118	0.154				
Area =	0.094	0.0670	0.078	0.090				

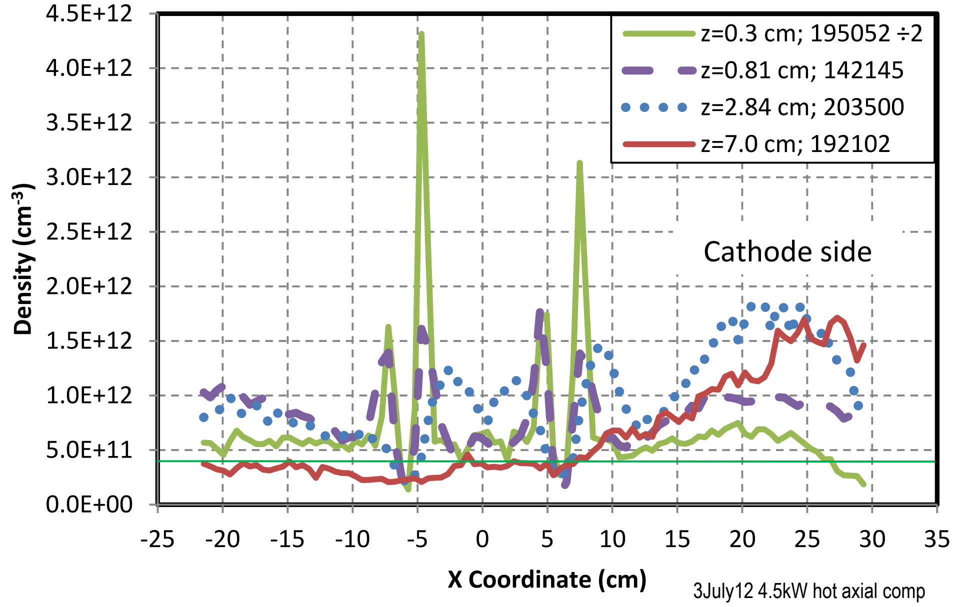

Figure 31. Collection of scans for horizontal pass along thruster midline, at 4.5 kW operating point. The spatial progression of the neutral jet atoms is apparent. Note that the z=0.3cm plot was divided by 2 and the horizontal green line denotes background neutral density in the facility.

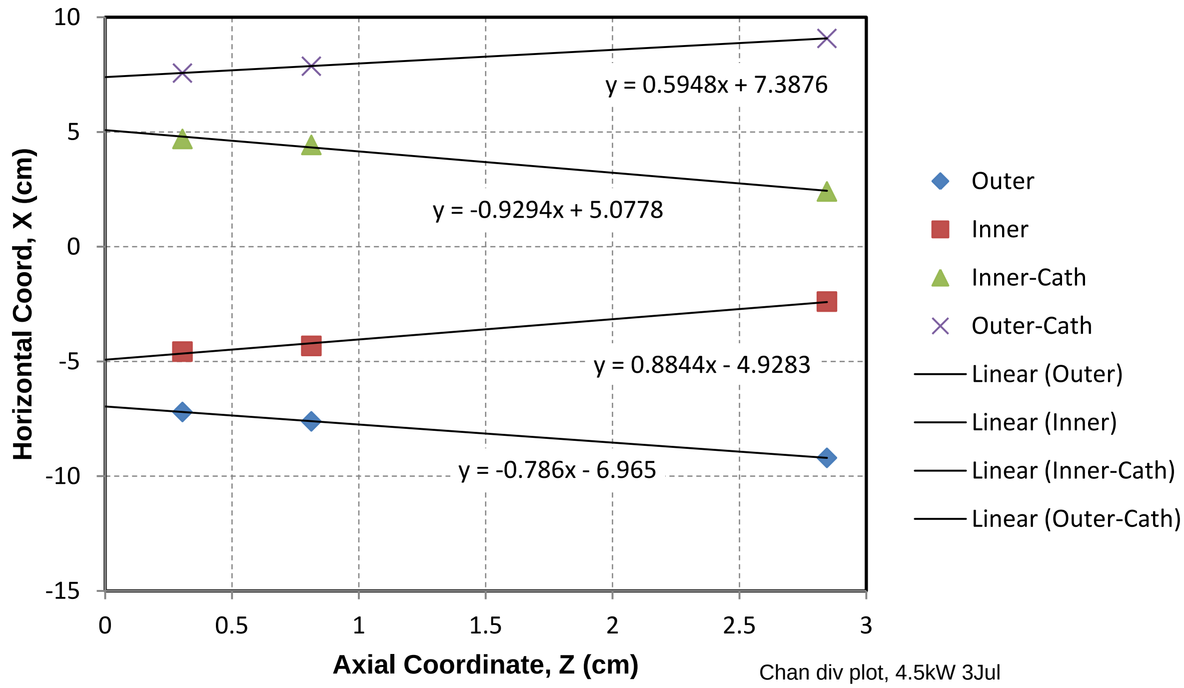

Figure 32. Divergence plots for emerging neutrals under 4.5 kW conditions, obtained from fitting peaks observed along thruster midline X-coordinate scan at several axial distances. Neutrals are primarily found near the inner and outer edges of the annulus in a jet-like, diverging flow. Data fits are extrapolated back to the exit plane.

Table 4. 4.5 kW x-axis profile fit results for y ≈ 0 cm and z=0.81 cm. The fit equation was y=y0+A*exp(-0.5((ν-ν_0)/w)^2), to allow convenient comparison to other results; a theoretical profile has not been established but would not be Gaussian. Data are plotted in Figure 31 and divergence behavior in Figure 32.

Parameter	Filename 142145	142145	142145	142145	Std Err 142145	Std Err 142145	Std Err 142145	Std Err 142145
Z (cm) =	0.81 cm	0.81 cm	0.81 cm	0.81 cm	0.81 cm	0.81 cm	0.81 cm	0.81 cm
Baseline (y0) =	6.04E11	4.88E11	5.46E11	5.45E11	8.3E10	9.1E10	9.3E10	5.6E10
Center (x_0) =	-7.613cm	-4.323	4.445	7.866	0.094	0.089	0.071	0.097
Width (Δx) =	0.491cm	0.539	0.421	0.568	0.11	0.11	0.076	0.11
A =	8.46E11	1.14E12	1.26E12	8.87E11	1.5E11	1.8E11	1.9E11	1.4E11
FWHM (Δx) =	1.156cm	1.269	0.991	1.337				
Area =	1.04E12	1.54E12	1.33E12	1.26E12				

Table 5. 4.5 kW x-axis profile fit results for y ≈ 0 cm and z=0.3 cm. The fit equation was y=y0+A*exp(-0.5((ν-ν_0)/w)^2) for convenient comparison to other results; a theoretical profile has not been established but would not be Gaussian. Data are plotted in Figure 31 and divergence behavior in Figure 32.

Parameter	Filename 195052	195052	195052	195052	Std Err 195052	Std Err 195052	Std Err 195052	Std Err 195052
Z (cm) =	0.3 cm	0.3 cm	0.3 cm	0.3 cm	0.3 cm	0.3 cm	0.3 cm	0.3 cm
Baseline (y0) =	4.56E11	4.60E11	5.13E11	4.92E11	7.5E10	7.19E10	7.6E10	3.2E10
Center (x_0) =	-7.196cm	-4.57	4.70	7.573	0.078	0.021	0.036	0.016
Width (Δx) =	0.347cm	0.298	0.305	0.364	0.066	0.024	0.10	0.015
A =	1.19E12	4.25E12	1.70E12	2.71E12	2.1E11	2.5E11	4.0E11	9.8E10
FWHM (Δx) =	0.818cm	0.701	0.718	0.858				
Area =	1.04E12	3.17E12	1.30E12	2.47E12				

Table 6. Calculated neutral jet divergence angles, relative to thrust axis, and FWHM for the four annular edges. Estimated error bars for θ are ±4 degrees.

Annular Edge	Intercept	Slope ($\Delta X_{pk}/\Delta Z$)	θ (degrees)	Slope ($\Delta X_{FWHM}/\Delta Z$)
Outer	7.388	0.595	30.7	0.665
Inner	5.078	-0.929	-42.9	1.059
Inner, cathode side	-4.928	0.884	41.5	0.996
Outer, cathode side	-6.965	-0.786	-38.2	0.811
Average absolute value		0.799	38.6	0.883

Table 7. Neutral jet calculated velocities.

X (cm)	$\Delta\nu_0$ (cm^{-1})	V_x (m/s)	V_z (m/s)	V_θ (m/s)
-7.19	0.0205	-367	460	589
4.70	0.0174	+312	390	500

Both inner and outer edges of the annulus are rounded, although the geometric details appear to be different. Therefore neutral atoms might diverge differently at the inner and outer edges. The divergence behavior of neutral jets at the annular edges is plotted in Figure 32; some of the lineshape fit results used to generate the plot are given in Tables 4 and 5. The peaks observed along midline x-coordinate scans, at three axial distances, were fitted to find peak position. Because the annular edges are located at approximately x= ±5 and ±7 cm, the plots converge to these values at the intercept. The slopes suggest that inner-edge neutrals may have a higher divergence angle than outer-edge neutrals. It would be interesting to see if inner and outer edge ion trajectories exhibit this difference.

The divergence angle for each jet is readily calculated from the data ($\arctan(\Delta x_{peak}/\Delta z)$), with results shown independently in Table 6 for each of the four annular edges. The average, about 39 degrees, is also computed. The Doppler shift measurements for the neutral jets were not performed exactly along the peak of the trajectory, but

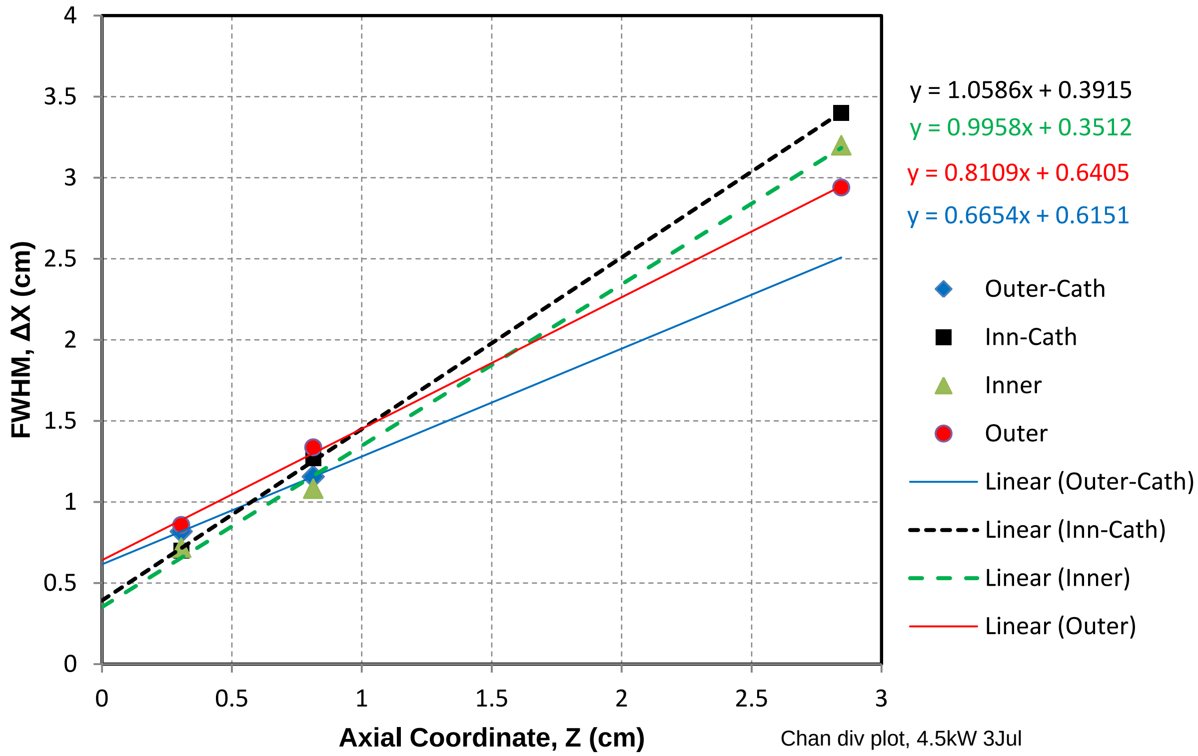

Figure 33. Full-Width-Half-Maximum Δx variation with axial coordinate.

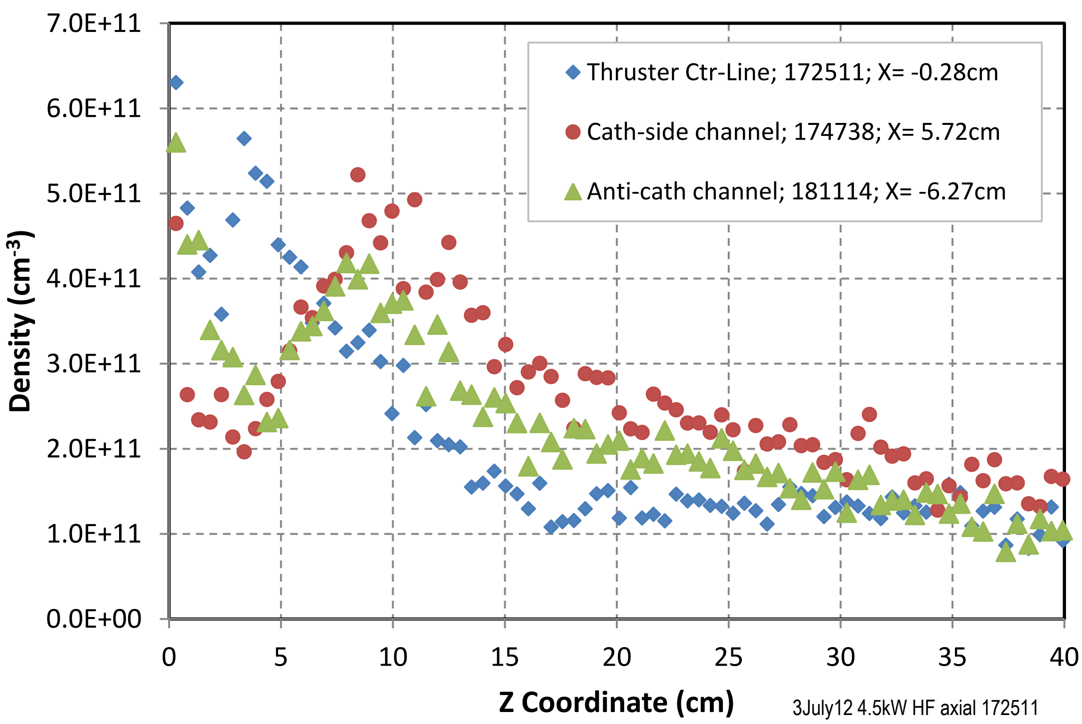

Figure 34. Axial neutral density results on thruster centerline and from horizontal cathode and anti-cathode side approximate mid-annulus positions, under 4.5 kW conditions. In each case, the thruster was translated along the z axis with y fixed at -0.13cm.

provide a useful means to estimate neutral jet velocity. Since the measurements closest to the trajectory peak were made at x= -7.19 and 4.70 cm, these are used for the velocity calculations. The x-component velocity is obtained directly from the measured Doppler shift, with z-component given by $v_x/\tan\theta$. The calculated velocity components and speed along the direction of travel, v_θ, are given in Table 7. The listed speed is similar to a previous measurement performed at the mid-channel of a 1-kW HET.[12]

The expression $(8kT/\pi m)^{1/2}$ gives the quantity $\bar{c}$, where $\bar{c}$ is the mean random velocity. If $\bar{c}/2$ gives the average directed velocity component v_z at the exit plane of the thruster, that component is about 105 m/s at 300K and 171 m/s (most probable value is 151 m/s) for an operating temperature of 800K. The mean directed velocity of the neutral jets is approximately 4 times higher than the room temperature figure. Since the random velocity increases with $T^{1/2}$, temperature on the order of 5,000K would be required – unlikely since thruster wall temperature is far lower.

Several mechanisms potentially influence the exit velocity of xenon neutrals at a Hall thruster exit plane. Ionization probability depends exponentially on the axial velocity component, which results in preferential ionization of the slowest neutrals.[12-13] The axial velocity distribution on which this mechanism acts is considerably broadened relative to room temperature and peaks at about 150 m/s. Ion impingement on the discharge chamber walls can produce energetic neutrals, although there is no direct measurement of velocity characteristics and flux for the situation of interest. Using an assumed accommodation coefficient and the preferential ionization mechanism mentioned, the mean velocity profile of on-axis xenon atoms from 15-mm inside the thruster to 50-mm outside was successfully modeled in a 1-kW class HET.[12] Ion-neutral interactions will also influence the neutral VDF, but Ref 12 concluded that its effect is relatively minor. Given that the model needs further validation and that the SPT-140 operates in a higher power regime, it is possible that charge exchange acceleration is important for the SPT-140. The directionality of the neutral jets coincides well with the presumed trajectory of ions exiting near the annular edge, which we take as evidence for ion-neutral charge exchange rather than ion-wall accommodation effects. Regardless, the high velocity lowers neutral density levels markedly (since F=nv; n=F/v) and will have significant effects on the breathing mode frequency and stability characteristics relative to values generally assumed in past modeling studies.

The full-width-half-maximum (FWHM) Δx value for the neutral jets is plotted in Figure 33, and increases at 67% to more than 100% of the Δz rate. The x-coordinate displacement of the neutral jet peak with increasing z also shows ≈1:1 correspondence, indicating that $\Delta x_{FWHM} \approx \Delta x_{pk}$ as z varies. The divergence *spread* of the neutral jets is therefore quite broad. Specific values for $\Delta x_{FWHM}/\Delta z$ are listed in Table 7, where there is no geometric correction related to the scan being linear rather than angular. Comparison of $\Delta x_{FWHM}/\Delta z$ and θ absolute values indicates they are well correlated. Inner-edge neutrals seem to have higher FWHM and larger divergence angle, with possibly lower axial velocity, but the differences are not statistically significant.

Neutral density results as a function of axial coordinate along 3 different paths are given in Figure 34. Each measurement was performed starting from horizontal mid-plane positions near the exit plane (y≈ -0.13cm), with the thruster translated from point to point along the z axis. For cathode and anti-cathode scans, neutral density varies most rapidly in the region very close to the exit plane (z = 0), passing through a minimum near z = 4 cm on both cathode and anti-cathode sides before rising to a maximum at about z = 10 cm that equals the background neutral density. The density falls monotonically from here to the end of the scan (z = 40 cm), at which point neutral density is roughly a third of the facility background level. There are differences between the cathode and anti-cathode scans. Near the exit plane, density is a bit higher on the anti-cathode side; this has been consistently observed on the various x-coordinate scans under both hot flow and cold flow conditions and may result primarily from higher gas flow rate on that side. The local minimum near z = 4 cm is nearly as deep, but displaced noticeably downstream relative to the cathode-side case. Its local maximum is displaced upstream relative to the cathode-side case. The z=4 minimum for the mid-channel scans may be due to efficient ionization occurring in that region. This behavior seems inconsistent with the idea of rapid source neutral slowing[12] and falling electron temperature, since these effects would increase the LIF signal.

During the axial scans a stripe formed on the collection mirror where its aluminum coating had been completely removed. This could potentially boost cathode side signal slightly relative to the subsequent anti-cathode side scan. It is not an adequate explanation of the difference between the traces. Similarly, the center-line scan was performed first but recorded the lowest density profile of the three, in the 7 to 40 cm range.

The background density of cold xenon neutrals in the facility is $\approx 4\times10^{11}$ cm^{-3}, considerably higher than the density at most measurement locations of Fig. 34. If the measurement is correct, it is evident that neutral depletion is occurring in the plume core in this region. Assuming that neutrals migrate inward from the background gas at large radius, and do not fully penetrate due to charge exchange reactions, it is reasonable to find lower density along the mid-field thrust axis than along the parallel lines emanating out from mid-channel positions. The centerline scan reaches the one-third-background baseline density already at z = 15 cm, much earlier than the others. This behavior might result from the attenuation of background neutral flux into the beam (due to charge exchange and scattering), ionization that extends out to large axial distances, high neutral temperature in the beam, or some combination of these factors. The center-line scan exhibits similarities, but the local maximum and minimum occur much closer to the exit plane. At z = 0 it is slightly above the facility background density, and drops nearly a factor of 2 within the first 2.5 cm downstream, where there is a minimum. The center-line maximum at z ≈ 4 cm stands in contrast to the minimum observed there during mid-annular scans, and may result from neutral jet convergence at that distance (see Figure 32). Density falls off in the downstream direction, presumably because of expansion and ionization effects.

A series of vertical passes made at various x coordinates near the exit plane is displayed in Figure 35. These show the familiar pattern of 4 peaks obtained during horizontal scans, corresponding to annular edge locations, for the smaller x values. For x = 4.80 cm, rather than observing two peaks for inner edge neutral jets, they are merged into a single, broad peak centered at y=0. This is because the laser interaction region moves along a tangent to the inner edge, and is therefore in contact with neutral jet emission over a considerable distance. For x = -5.36 cm, the inner edge jets are almost completely missed, and just two prominent peaks are observed – corresponding to outer edge jets. These peaks are broad relative to all other cases except x = -7.90 cm, because the jet and laser beam directions are better aligned. For x = -7.90 cm, jet and laser directions are anti-parallel with the laser interaction moving along a tangent to the outer edge, and further broadening occurs. Peak shape broadening will always occur when the traversal has a component that is tangent to the annulus. Annular edges are encountered at larger absolute y values for the x = -0.28 cm case, compared to x=2.26 and -2.82 cm data, because the curvature of the annulus moves the latter peak positions toward the center of the plot.

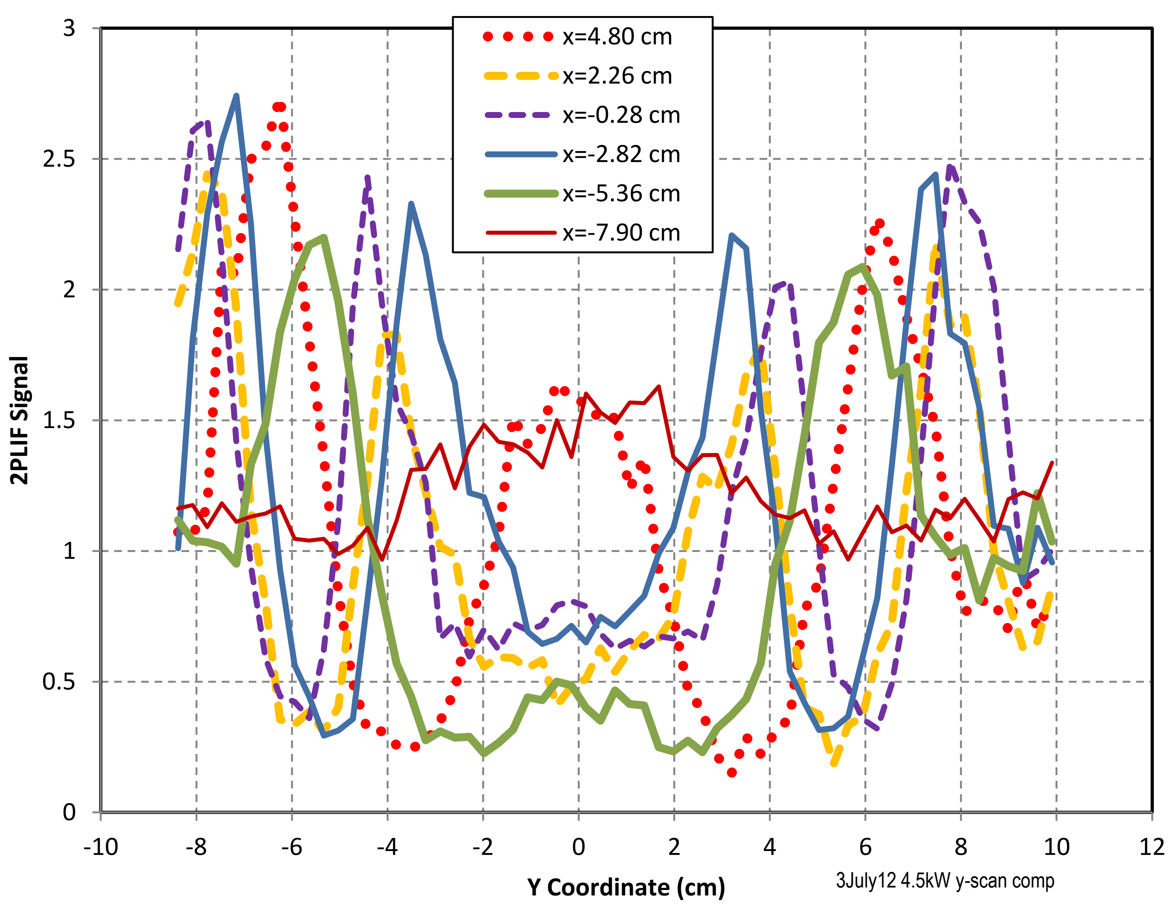

Figure 35. Collection of scans for vertical passes with various X values at 4.5 kW operating point, Z=0.81cm.

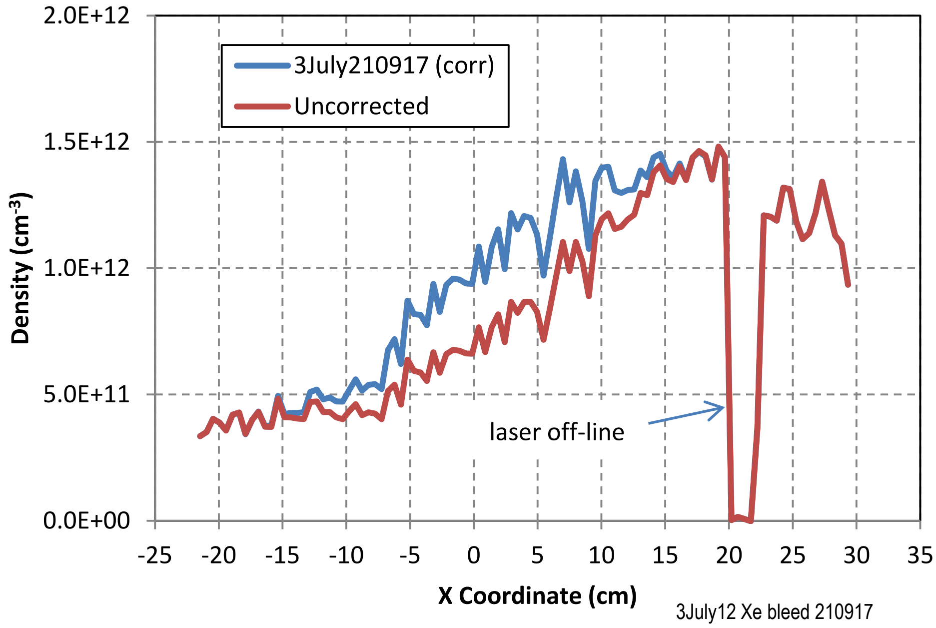

Figure 36. Dependence of baseline pressure on x coordinate with thruster off and external xenon bleed on, and Z=2.84cm. Asymptote at large negative x agrees well with reading of the wall-mounted ion gage nearest the thruster, which corresponded to the value normally obtained for 4.5 kW hot or cold flow conditions. Laser off-line results confirm that the signal is entirely due to neutral xenon.

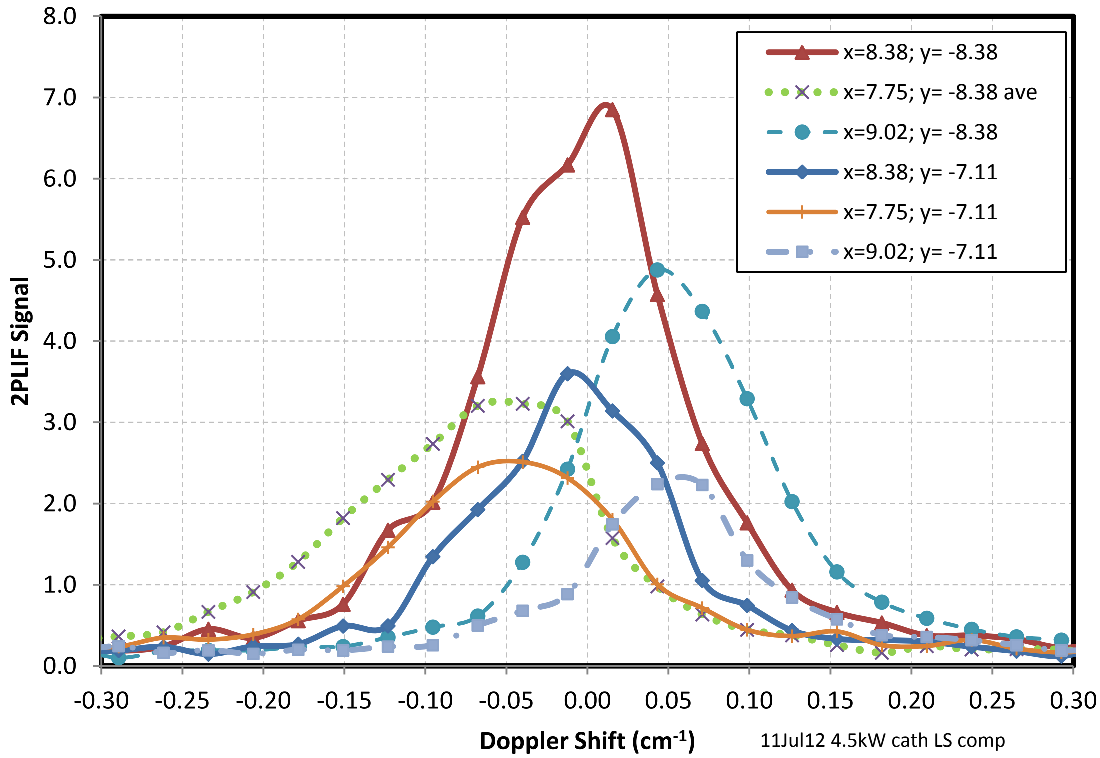

Figure 37. Collection of lineshapes for cathode at 4.5 kW operating point; smoothed signal traces plotted vs. frequency, no fit results shown.

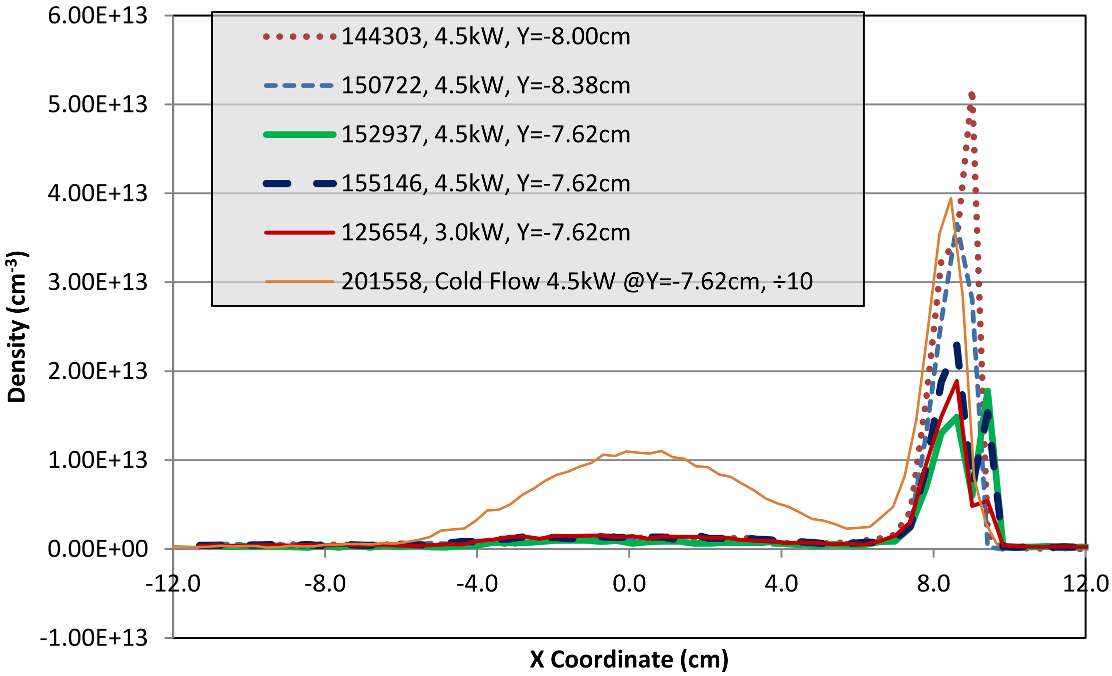

Figure 38. Collection of cathode neutral density profiles obtained from series of horizontal thruster scans at various heights. The cold flow density was divided by 10 for convenient comparison.

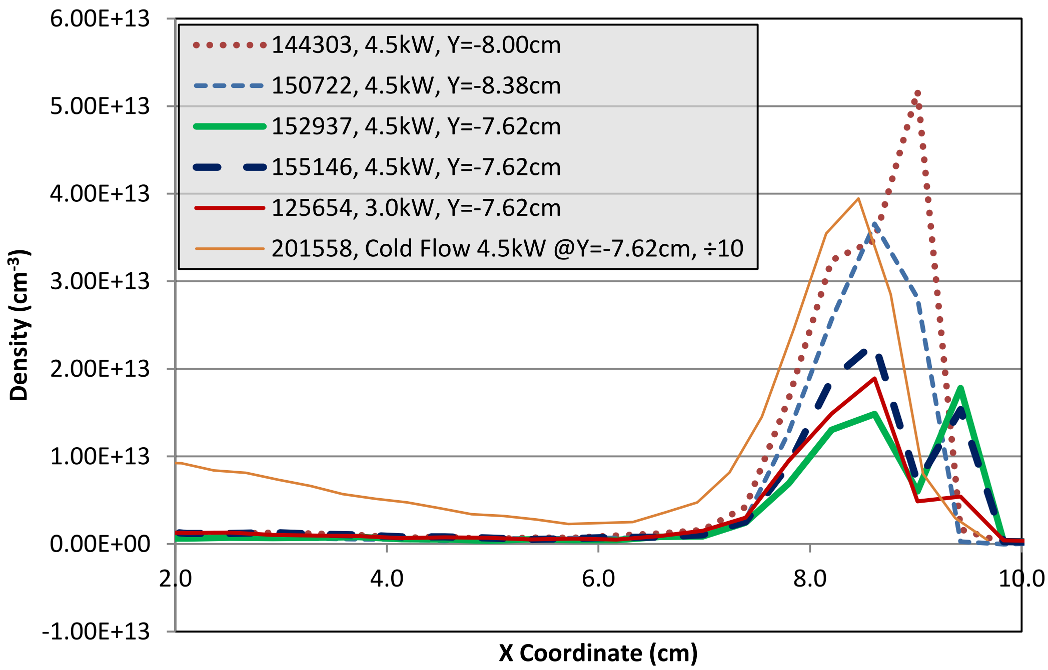

Figure 39. Collection of cathode profiles from Fig. 4-38 with expanded x axis.

Neutral xenon baseline level was measured along a horizontal mid-plane cut at z=2.84 cm during xenon bleed into the vacuum tank from an external source. Verification that the signal was due to neutral xenon was made by temporarily setting the laser frequency off-line. The baseline depended significantly on thruster position, as shown in Figure 36, indicating that the thruster body location somehow influences local density distribution without xenon flowing through thruster anode or cathode. The baseline here could be similar to the underlying baseline for the z=2.84 cm scan plotted in Figure 31; the z=7.0 cm case obviously has some similarities. In that Figure a gradually decreasing density with axial coordinate is evident for translation toward large negative x, and a gradually rising density at increasing, positive x values that is maximized around x=20 to 25 cm. This result is difficult to explain, but the most likely cause seems to be a transport effect combined with thruster system hardware acting as a "stop" or scattering site for neutrals and causing neutral density pileup. Neither in-vacuum leaking from the propellant line nor mirror obscuration/reflectivity can explain the observation. Significant net neutral transport occurs from downstream to upstream chamber regions, driven by the density gradient that is established by far-field ion beam impact on beam stop and other surfaces during thruster operation. Similarly, the xenon bleed was directed upstream at the thruster from a side port. In addition to front pole piece and insulator surfaces, the cathode assembly mounted on one side of the thruster and its mounting system – including two "ears", are among the potential "stop" surfaces that translate with the positioning system. There is substantial impingement surface area for neutral pileup near the laser interaction region over the x= -10 to +20 cm range.

Measured lineshape profiles at various locations near the exit plane of the hollow cathode are plotted in Figure 37, with z=1.68 cm for each case. It is obvious that neutrals are emitted from the cathode with high velocity, considerably higher than in the case of the neutral jets at the exit plane of the thruster. For x=8.38 cm, the Doppler shift is minimal – as observed for both y= -8.38 and -7.11 cm cases. This x coordinate approximately corresponds to a plane parallel to the thrust axis, encompassing both cathode orifice and laser interaction region. The signal is relatively high for x=8.38, y= -8.38 cm, because it approximately corresponds to the minimum distance from orifice exit to interaction region, despite being off-axis with respect to the cathode plume expansion. To be more precise, based on the measured geometry the minimum distance corresponds to $x_0=y_0=8.13$ cm ±0.15 cm. The cathode is canted 30 degrees toward the thrust axis, with plume direction such that $\Delta x= -\Delta y = \Delta z/\sqrt{6}$, and $\Delta z' = 1.155\Delta z$, where z' is the distance from orifice to laser interrogation region along the cathode beam axis and z is the distance along the thrust axis. A +1 cm displacement away from the laser interaction region, along the thrust axis direction, requires -0.41 and +0.41 cm displacements along x and y, respectively, to keep the cathode axis aligned with the interaction region and puts the orifice 1.16 cm further from the interrogation point. If z'=1.16 cm, we calculate x=7.72 and y= -7.72 cm to align cathode axis with interaction region. In practice, the z' coordinate is not accurately known. It is important to note here that if the cathode plume does not expand collinearly with the axis of the orifice channel, the optimal x, y displacements can be affected.

The lineshape for some of the cathode scans, particularly those with a blue shift (positive peak Δν with respect to "zero"), is asymmetric with larger than typical width (FWHM). It is not surprising that these lineshapes would be more Doppler broadened, since the blue-shifted profiles have a larger velocity component along the axis of laser propagation. A Doppler shift of 0.05 cm^{-1}, observed for several of the lineshape scans, corresponds to a directed velocity component in the laser beam direction of about 900 m/s. The orifice position is not precisely known, but presuming the angle between laser beam and neutral trajectory to be 65 degrees we estimate 1.6 km/s for the neutral speed. Considering the cathode as a supersonic neutral beam source with high stagnation temperature and taking $\sqrt{5kT_0/m}$ as the maximum terminal velocity,[14] exit velocity equal to 1.6 km/s corresponds to T_0 ~ 10,000K. The stagnation temperature of neutrals should be much lower and we conclude that another neutral acceleration mechanism is at work, as in the case of the neutral jets emerging from the thruster annulus. That mechanism may involve ion-neutral collisions. Charge exchange collisions that transfer little momentum between nuclei are highly effective in creating energetic neutrals, and scattering collisions are also important.[15-16] For this mechanism to be effective, ion flux and ionization fraction must be high and emitted ions must have substantial energy - conditions that can be realized with a hollow cathode under some circumstances, and at the exit plane of the thruster annulus routinely.[17-18] The largest peak Doppler shift for the profiles shown, about 0.06 cm^{-1}, occurred in the x=9.02, y= -7.11 cm case. It is a blue shift because the cathode has traveled past the laser interaction region, and atoms moving in the direction of laser propagation are being monitored.

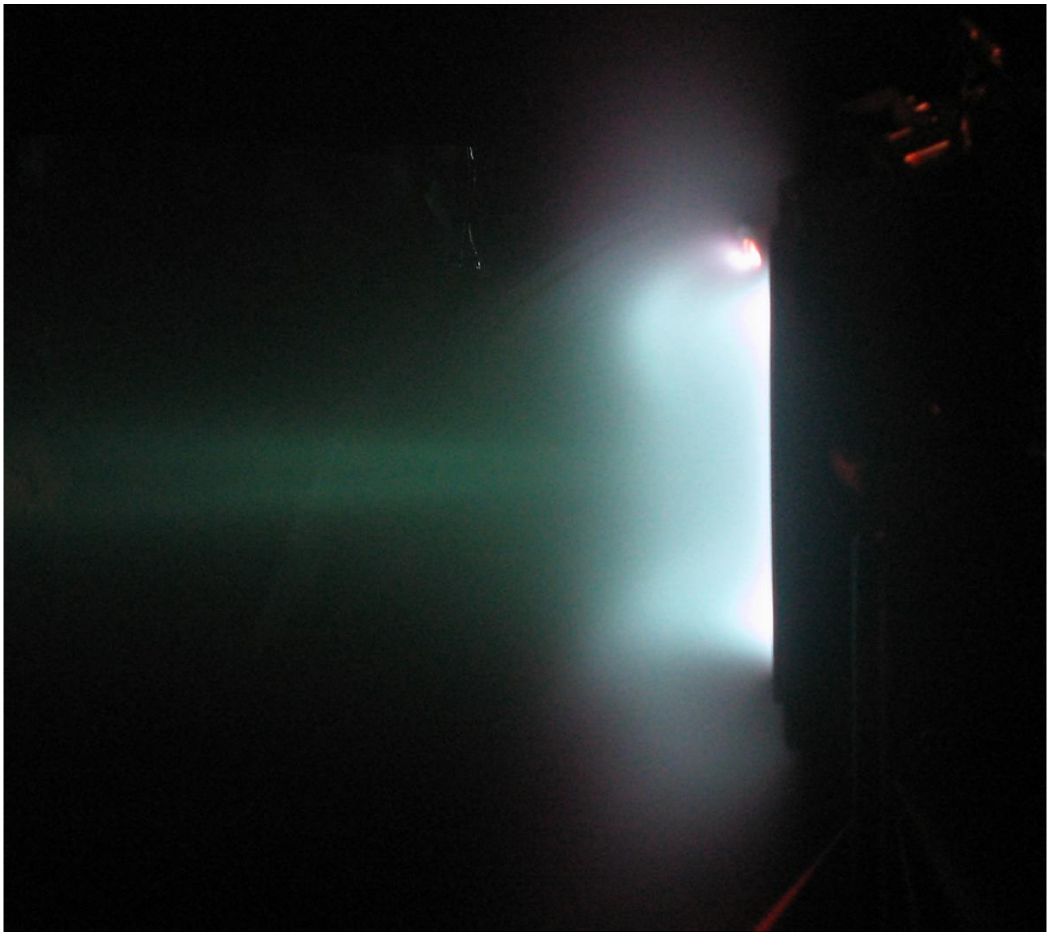

Figure 40. Image of operating thruster, showing plume “jet” and slight asymmetry associated with cathode.

Figure 41. Expanded image (from Figure 40), showing the apparent 90 degree “turn” of luminous plasma generated by the cathode, together with “halo” and possible “streamlines”.

The "turn" executed by the luminous cathode plume, seen in Figures 40 and 41, may further affect neutral velocity profiles. It is believed to be a manifestation of cathode electrons following the local magnetic field lines. There also seems to be a suggestion of plasma streamlines arcing into the ion beam of the thruster further downstream; this plasma is also associated with the cathode. The less intense "halo" emission at radii larger than the core plume emission, may be associated with emitted cathode electrons spiraling around divergent field lines outside the separatrix. This halo can be expected to vanish in the case of a center-mounted cathode.[11] The profile for x=9.02, y=-8.38 cm appears to be obtained within the turned plasma region. The lineshape is quite symmetric and about the same width as the laser lineshape, as is the profile for x = 9.02, y=-7.11 cm, indicating that species velocities have modest magnitudes. In contrast, the x=7.75, y=8.38 cm profile in Figure 37 is obviously distorted, with a sharp rise on the low velocity side and an apparent exponential tail on the high velocity side. This observation is consistent with the ion acceleration mechanism mentioned, which is expected to produce an exponential tail on the high velocity side. Strong ion-induced acceleration and favorable laser beam orientation with respect to it may explain the high degree of lineshape distortion. It should also be noted that the profiles have not been deconvolved from the laser lineshape profile to yield their velocity distribution functions.

One previous study measured a high neutral exit velocity for a cathode in an operating Hall thruster[19] (cathode studies that measure neutral exit velocity are extremely rare). Neutral "temperature" of about 2500K was found - also higher than cathode wall temperature and the presumed stagnation temperature. The directed velocity was approximately 1500 m/s, very similar to the present finding, but no explanation for this high figure was given.

In the presence of a thruster ion beam, cathode emission normally rises significantly at a given flow rate. This coupling between cathode and ion beam may elevate the ionization fraction and increase the amplitude of the potential hill. Despite the high exit velocity, neutral density near the cathode still dominates density measurements in the thruster plume. The observation strongly suggests the presence of a "hill" downstream from the orifice, with enough positive plasma potential to accelerate ions and (indirectly) neutrals.

A series of horizontal scans near the height of the cathode orifice was executed, with results shown in Figure 38. Figure 39 is the same plot with expanded scale for the region of interest. Results show a peak shift toward higher x coordinate for hot flow, relative to cold flow. The hot flow profiles corresponding to y= -7.62 cm appear to be split into two peaks centered at x = 8.6 and 9.4 cm. The latter peak implies cathode emission at a large angle away from the thrust axis. This angle is smaller for y= -8.00 and -8.38 cm cases, where a single peak or peak with a shoulder is observed and no signal was recorded for $x \geq 9.4$ cm. The data strongly suggest that where neutrals go is affected substantially by the cathode plasma dynamics during operation. Neutral speed distribution is also affected. Turning of the exiting plasma by the local magnetic field is probably an influential factor.

V. Xenon Neutral 3-kW Hot Flow Measurements

Data were also obtained at the standard 3-kW operating point, although at slightly different coordinates with respect to 4.5-kW results. Only rough comparisons can therefore be made between the two power levels. As in the 4.5-kW case there are measurable peak Doppler shifts. The magnitudes of the peak shifts are similar at 3 and 4.5-kW, and the power dependence of the shift (see fit results in Table 8) may not be statistically significant. 3-kW data of this type were only obtained at one z coordinate, in contrast to the high power case. Outer-edge divergence may be larger than inner-edge at the low power setting, as it appeared to be at high power, but the data are not definitive.

Lineshapes obtained for neutral jets at annular edges along the vertical were also obtained, with z = 0.9 cm and x = -0.28 cm. The results are plotted in Figure 44. The fitted profile widths are larger than typical laser line width profiles, but this may be attributable to other factors such as poor signal to noise ratio. Significant Doppler broadening would not be expected for these data.

Lineshapes obtained near the hollow cathode are plotted in Figure 46, and exhibit some differences with respect to the 4.5-kW case. Profile widths tend to be less than observed at the high power setting and the variation of peak Doppler shift may also be a little less. There is no obvious distortion of profile, with the possible exception of x=8.38, y= -7.11 cm.

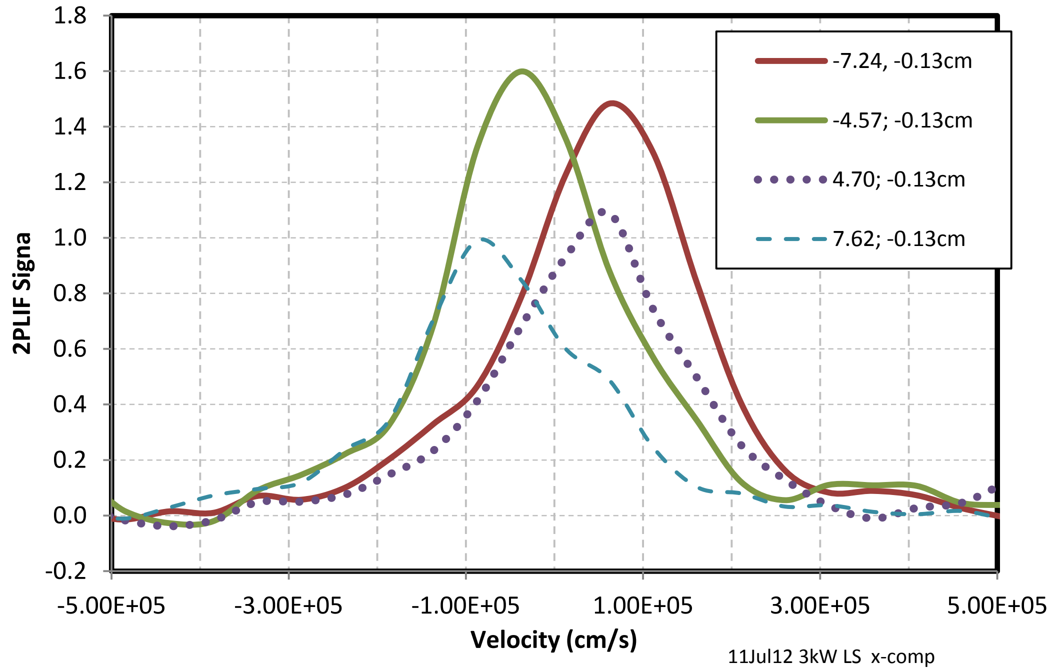

Figure 42. Lineshape comparison for 3 kW operating point at four locations along a horizontal midline cut with Z= 0.15cm. Smoothed signal traces are plotted vs velocity rather than frequency.

Table 8. 3-kW peak fit results (11Jul) for hot flow X-axis scan, z = 0.15 cm and y=-0.13cm, based on wavenumber abscissa rather than velocity, Gaussian Amplitude profile (y=y0+A*exp(-0.5*((x-xc)/w^2))). The data are plotted in Figure 42 vs a velocity abscissa, with fit vs frequency given in Figure 43.

Parameter	**Filename**				**Standard Error**			
	141832	**142903**	**143932**	**145303**	**141832**	**142903**	**143932**	**145303**
X (cm)	-7.24	-4.57	4.70	7.62	-7.24	-4.57	4.70	7.62
y0	0.035	0.057	0.023	0.022	0.015	0.018	0.012	0.012
Center (ν_{01})	0.0342	-0.0155	0.0245	-0.0352	0.0017	0.0019	0.0019	0.0022
Width ($\Delta\nu_1$)	0.0536	0.0505	0.0546	0.0560	0.0018	0.0021	0.0022	0.0024
A	1.403	1.490	0.986	0.889	0.039	0.049	0.031	0.031
FWHM (cm^{-1})	0.1261	0.1190	0.1286	0.1319	-	-	-	-
Area	0.188	0.189	0.135	0.125	-	-	-	-

Table 9. 3.0 kW peak fit results (11Jul) for hot flow x-axis scan, z = 0.15, based on velocity abscissa rather than frequency, using same data as Table 8 and Fig 42. A Gaussian Amplitude profile (y=y0+A*exp(-0.5*((x-xc)/w^2)))) was assumed.

Parameter	**Filename**				**Standard Error**			
	141832	**142903**	**143932**	**145303**	**141832**	**142903**	**143932**	**145303**
X (cm)	-7.24	-4.57	4.70	7.62	-7.24	-4.57	4.70	7.62
y0	0.035	0.057	0.023	0.022	0.015	0.018	0.012	0.012
Center (cm/s)	61303	-27749	43927	-62965	2948	3335	0.0019	0.0022
Width (cm/s)	95932	90496	97780	100286	3272	3670	0.0022	0.0024
A	1.403	1.490	0.986	0.889	0.039	0.049	0.031	0.031
FWHM (cm/s)	225904	213102	230255	236156	-	-	-	-
Area	337471	337891	241643	223389	-	-	-	-

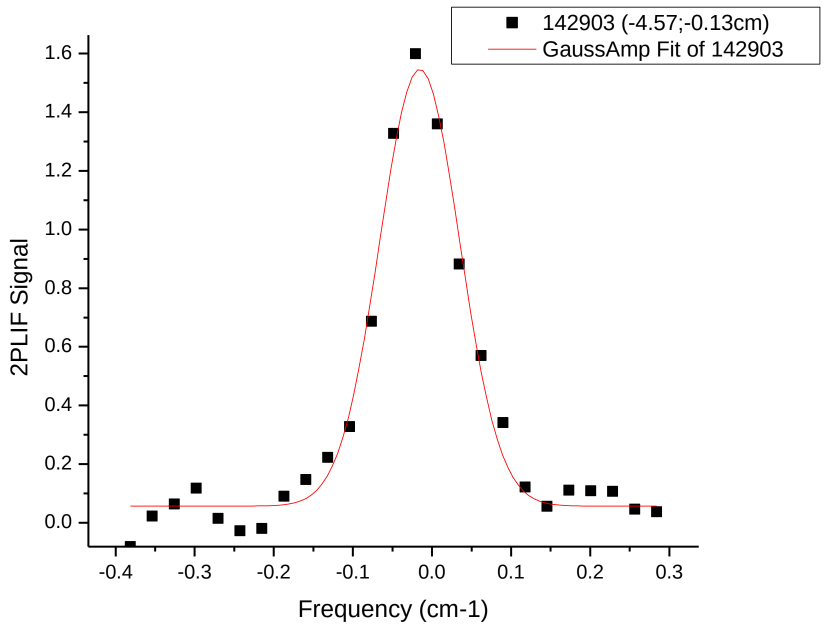

Figure 43. Example Gaussian Amplitude lineshape fit for 3 kW operating point at x = -4.57 cm, y = -0.13 cm, z = 0.15 cm. Data are also plotted in Figure 42.

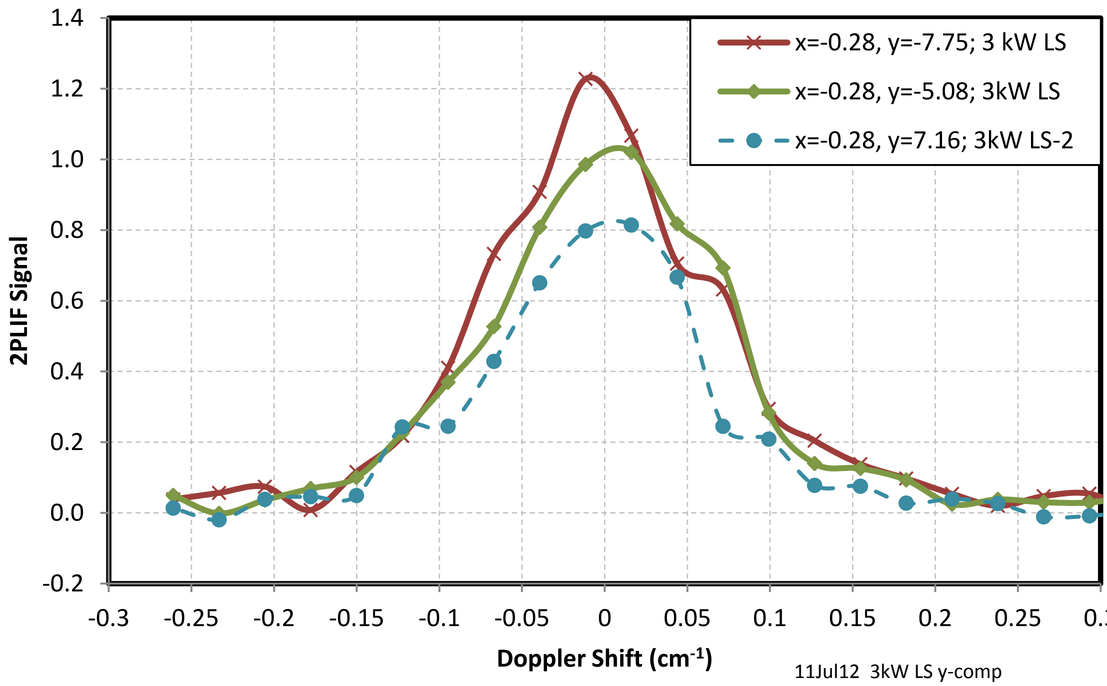

Figure 44. Comparison of 3 kW smoothed lineshapes obtained along a vertical line at the indicated coordinates.

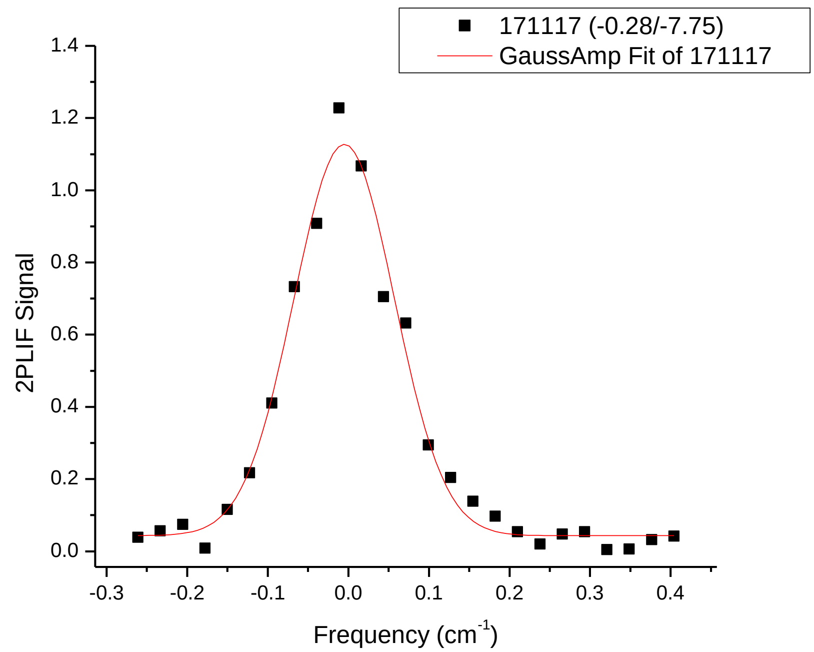

Figure 45. Example Gaussian peak fit of 171117 file.

Table 10. 3 kW y-axis lineshape fit results (11Jul) for x = -0.28 cm and z = 0.15 cm. The fit equation was y=y0+A*exp(-0.5((x-xc)/w)^2). An example fit is given in Figure 45 and data are compared in Figure 44.

Parameter	**Filename**				**Std Err 117117**	**Std Err 172403**	**Std Err**	**Std Err 175233**
	171117	**172403**		**175233**				
Y (cm) =	-7.75	-5.08		7.16				
Baseline (y0) =	0.043	0.042		0.018	0.014	0.011		0.013
Center (v_0) =	-0.0051	0.0039		-0.0033	0.0021	0.0017		0.0025
Width (Δv) =	0.0623	0.0636		0.0583	0.0024	0.0020		0.0029
FWHM (Δv) =	0.1466	0.1497		0.1373				
Height =	1.084	0.978		0.801	0.033	0.024		0.031
Area =	0.1692	0.1558		0.1170				

Lineshapes were also obtained at medium and large positive and negative x coordinates to check for Doppler effects to the side of the thruster. These data are plotted in Figure 47, together with a measured cold flow lineshape. Fitted lineshape results are given in Tables 11 and 12. The data are not able to reveal any lineshape variations with the x coordinate, of course, because the profile is dominated in each case by laser linewidth - masking any underlying Doppler effects. There does appear to be a bias at medium distance toward red-shifting of the peak position on one side of the thruster and blue-shifting on the other, suggesting that neutral velocity is directed toward the thrust axis from both sides. This is to be expected if neutral depletion is occurring in the plume.[8-9] Results are shown pictorially in Figure 48. As concluded from various X-scan profiles near the exit plane, the xenon neutral density is very low near the center of the annulus and, except for the neutral jets emanating from the annular edges, typically trends higher with increasing distance from the thrust axis. This is observed in Figure 48 as well.

Neutral depletion has been observed previously in helicon discharge plasmas, where neutral migration into the discharge region is believed to result.[8-9] Plasma and neutral gas pressure gradients exist, with electron-neutral collisions acting as a drag on neutral migration into the high density plasma regions. Doppler shifts listed in Table 11, based on fitted peak position at each location, have high error margins due to the modest signal to noise ratio and

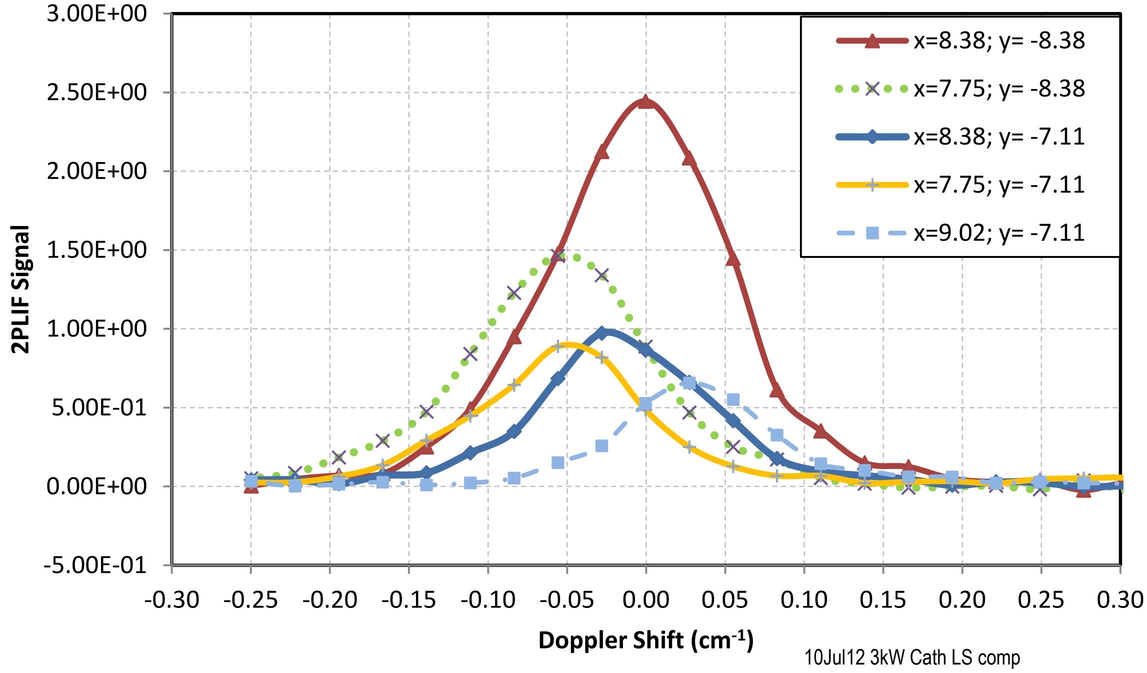

Figure 46. Comparison of lineshapes obtained near cathode, for 3 kW operating point and z=0.15 cm.

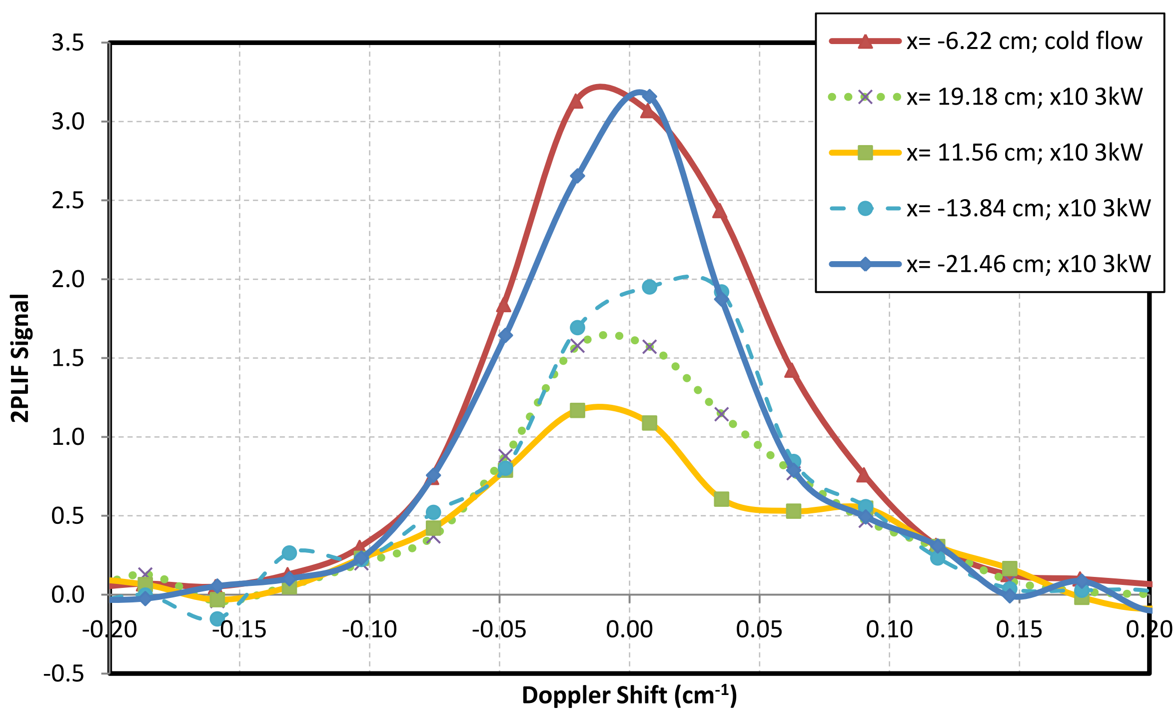

Figure 47. Lineshapes for various x coordinates near exit plane, compared with a cold flow lineshape.

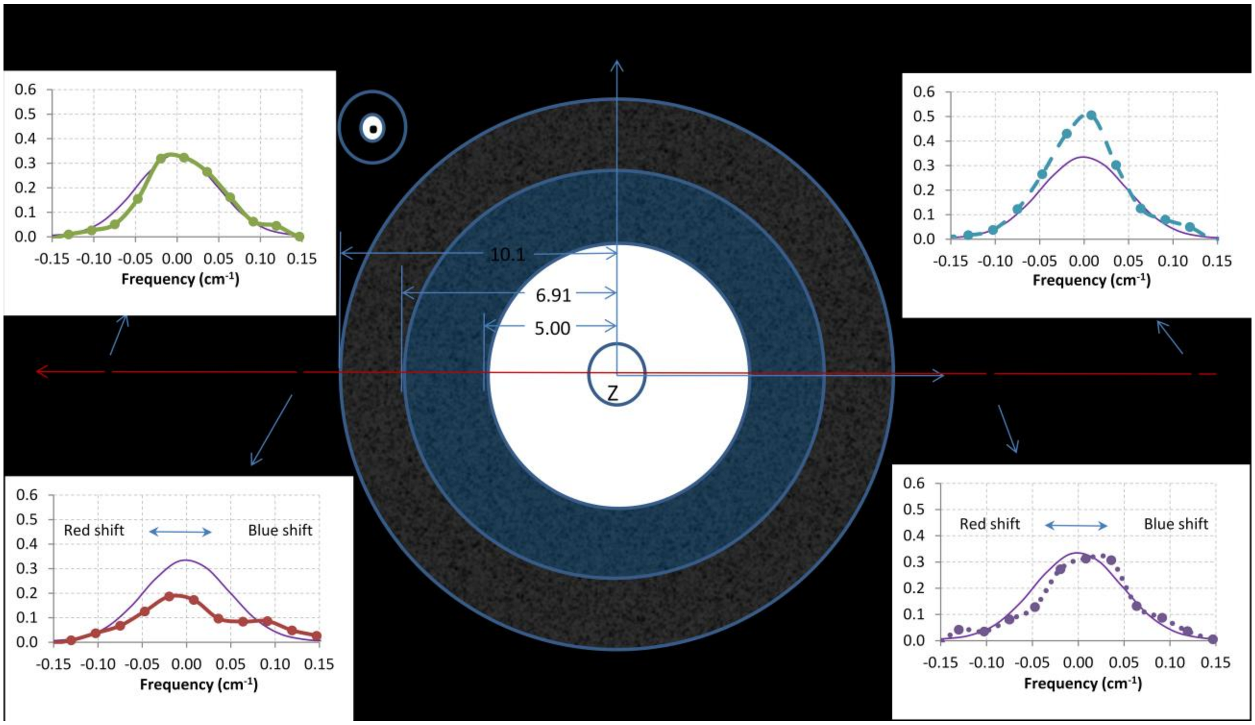

Figure 48. Hot flow 3kW lineshapes for various X coordinates near the SPT-140 exit plane, as indicated in Figure 47, diagramming their locations in relation to the thruster (the annulus is blue-shaded). In each case the fitted cold flow lineshape (solid line) is shown for comparison with the new data points (solid circles).

Table 11. Doppler shift results for data shown in Figure 47 (3 kW (11Jul) data for x = -0.28 cm and z = 0.15 cm; fit equation y=y0+A*exp(-0.5((x-xc)/w)^2)).

Parameter	**Filename**			
	153435	**152503**	**150332**	**151502**
X (cm) =	-21.5	-13.8	11.6	19.2
Center (v_0) =	~0	≤ 0.01	≥ -0.01	~0

dominance of laser lineshape. A peak Doppler shift of 0.0055 cm^{-1} would correspond to directed velocity of about 100 m/s, which is more than half the mean thermal velocity of the background gas. Doppler shift of 0.01 cm^{-1}, as suggested by Table 11, exceeds the mean thermal velocity at 300K and may be less feasible to achieve.

VI. Conclusions

Neutral density measurements were performed under cold flow conditions and under hot flow conditions at standard 3 and 4.5 kW operating points. Neutral density results under cold flow conditions indicated significant density and flux asymmetry between left and right sides of the annulus at the horizontal mid-line. Averaging out the asymmetry in the density data and integrating the differential flux based on azimuthal symmetry to obtain a total mass flux figure, a close match was obtained with the known anode mass flow rate.

Average hot flow neutral density across the thruster mid-line exit plane was nearly two orders of magnitude below the cold flow result, consistent with high ionization efficiency and elevated exit velocity under hot flow conditions. Neutral density was found to vary strongly across the face of the operating thruster, with prominent peaks at inner and outer edges of the annulus, and highest density near the hollow cathode orifice. The former peaks, which are due to jets of fast-moving divergent neutral atoms, may be related to electron density variations. The neutral jets have substantial divergence, with beam center pointed well away from the thrust axis. The jet velocity is much higher than calculated based on expected anode or thruster wall temperatures. The elevated velocity may stem from the combined effects of preferential ionization of slow neutrals, accommodation effects of ion-wall collisions, and ion-neutral collisions. A similar explanation may apply to the observation that neutral exit velocity from the cathode is even higher than found at the thruster exit plane. If ion-neutral charge exchange is an important determinant of neutral exit velocity, the peak of the neutral jet distribution should coincide closely with the trajectory of ions exiting from the same location near the annular edge, as seems to be the case. Thruster models generally assume substantially lower neutral exit velocities (associated with higher density) than measured here. Neutral density may strongly influence time-dependent behavior, including thruster stability characteristics.

Axial scans starting from the middle of the annulus, during 4.5 kW operation, revealed complex behavior - including rapidly falling density at the annular exit, local minimum at 4 cm that is well below chamber background and maximum at 10 cm. From the local maximum there is a gradual tail-off to below background density levels. These observations suggest that neutral depletion is occurring in significant portions of the plume and that a neutral ionization mechanism is active in the plasma flow traveling away from the exit plane. Electron impact ionization and/or ion-neutral collisions are the likely causes of the neutral depletion. Cold background gas in the test facility diffuses into the ion beam over its length, acting to partially replenish what is lost. Conversion of fast ions into slower ions via ion-neutral collisions and subsequent acceleration in the local electric field may increase total plume momentum and registered thrust.[20-21]

Acknowledgments

This project was supported by Space Systems/Loral under Contract BPA 3221 to The Aerospace Corporation. The authors thank Jim Pollard for technical discussion and Kristina Jameson for assistance with thruster operation.

References

1. Crofton, M.W., "Measurement of Neutral Xenon Density Profile in an Ion Thruster Plume," AIAA Paper 96-2290, 27th AIAA Plasmadynamics and Lasers Conf., June 1996, New Orleans.
2. Eichhorn et al, "Two-Photon Laser-Induced Fluorescence of Neutral Xenon in a Thin Xenon Plasma," *Journal of Propulsion and Power* 28, No. 5, September-October 2012, pp. 1116-20.
3. Walker, M.L. and Gallimore, A.D., "Neutral Density Map of Hall Thruster Plume Expansion in a Vacuum Chamber," *Review of Scientific Instruments*, 76, 053509 (2005).
4. Friedrich, D.M., "Two-Photon Molecular Spectroscopy," *Journal of Chemical Education* 59, No 6 (1982), pp. 472-481.
5. Halfmann, T., Rickes, T., Vitanov, N.V., and Bergmann, K., "Lineshapes in Coherent Two-Photon Excitation," *Optics Communications* 220 (2003) 353-359.
6. Pawelec, E., Mazouffre, S., and Sadeghi, N., "Hyperfine Structure of some Near-Infrared XeI and XeII Lines," *Spectrochimica Acta Part B* 66 (2011), pp. 470-475.
7. Hargus, W.A. Jr and Cappelli, M.A., "Laser-Induced Fluorescence Measurements of Velocity within a Hall Discharge," *Applied Physics B* 72 (2001), pp. 961-969.
8. Aanesland, A. et al, "Direct Measurements of Neutral Density Depletion by Two-Photon Absorption Laser-Induced Fluorescence Spectroscopy," *Applied Physics Letters* 91, 121502 (2007).
9. Fruchtman, A., Makrinich, G., Chabert, P., and Rax, J.M., "Enhanced Plasma Transport due to Neutral Depletion," *Physical Review Letters* 95, 115002 (2005).
10. Mikellides, I.G., Katz, I., Hofer, R.R., Goebel, D.M., de Grys, K., and Mathers, A., "Magnetic Shielding of the Acceleration Channel Walls in a Long-Life Hall Thruster," AIAA Paper 2010-6942, 46th Joint Propulsion Conference, Nashville, July 25-28 (2010).
11. Hofer, R.R., Johnson, L.K., Goebel, D.M., and Fitzgerald, D.J., "Effects of an Internally-Mounted Cathode on Hall Thruster Plume Properties," AIAA Paper 2006-4482, 42nd Joint Propulsion Conference, Sacramento, 9-12 July (2006).
12. Mazouffre, S., Bourgeois, G., Garrigues, L., and Pawelec, E., "A Comprehensive Study on the Atom Flow in the Cross-Field Discharge of a Hall Thruster," Journal of Physics D: Applied Physics, Vol. 44, 2011, p. 105203.
13. Hargus, W.A. Jr and Capelli, M.A., Journal of Propulsion and Power 18 (2002), 159.
14. Christen, W., Rademann, K., and Even, U., "Supersonic Beams at High Particle Densities: Model Description beyond the Ideal Gas Approximation," *Journal of Phyical Chemistry A* 114 (2010), 11189-11201.
15. Boyd, I.D., and Yim, J.T., "Modeling of the Near Field Plume of a Hall Thruster," *Journal of Applied Physics* 95, No. 9, May 2004, pp. 4575-4584.
16. Katz, I., Jongeward, G., Davis, V., Mandell, M., Mikellides, I., Dressler, R., Boyd, I., Kannenberg, K., Pollard, J., and King, D., "A Hall Effect Thruster Plume Model including Large-Angle Elastic Scattering," AIAA Paper 2001-3355, 37th Joint Propulsion Conference, 8-11 July (2001).

17. Crofton, M.W., “Preliminary Mass Spectrometry of a Xenon Hollow Cathode,” *Journal of Propulsion and Power* 16(1), pp. 157-159 (1999).
18. Foster, J.E. and Patterson, M.J., “Characterization of Downstream Ion Energy Distributions from a High Current Hollow Cathode in a Ring Cusp Discharge Chamber,” AIAA Paper 2003-4865, 39th Joint Propulsion Conference, Huntsville, 20-23 July (2003).
19. Williams, G.J. Jr., Smith, T.B., Glick, K.H., Hidaka, Y., and Gallimore, A.D., “FMT-2 Discharge Cathode Erosion Rate Measurements via Laser Induced Fluorescence, AIAA Paper 2000-3663, 36th Joint Propulsion Conference, 17-19 July (2000).
20. Crofton, M.W. and Pollard, J.E., “Thrust Augmentation by Charge Exchange,” 49th AIAA/ASME/SAE/ASEE Joint Propulsion Conference, San Jose, 14-17 July (2013).
21. Crofton, M.W. and Boyd, I.D., “Momentum Modeling of a Hall Thruster Plume,” IEPC Paper 2013-374, 33rd International Electric Propulsion Conference, Washington DC, October 2013.